Validation of NeQuick topside ionospheric formulation using selected COSMIC/FORMOSAT-3 data and possible improvements

Arun Kumar Singh[2], Haris Haralambous[1, 2], Christina Oikonomou[2]

1. Department of Electrical Engineering, Frederick University, Nicosia, Cyprus
2. Frederick Research Center 7 Filokyprou Street, Pallouriotissa 1036, Nicosia, Cyprus

Corresponding author Email: arsurya123@gmail.com

Key Points:

- α-Chapman and Corrected NeQuick underestimate, whereas IRI-NeQuick overestimates COSMIC topside electron density measurements.
- Corrected NeQuick provides a better topside representation among all three topside formulations.
- Corrected NeQuick topside formulation further improves with an optimised value of g = 0.15.

Abstract

We examine systematic differences between topside electron density measurements and different topside model formulations including ground-based α-Chapman extrapolated topside electron density profiles from auto scaled ionograms, International Reference Ionosphere Model (IRI-2016) NeQuick topside estimations and a recently improved NeQuick (Corrected NeQuick) topside formulation. The selected topside electron density measurements considered were taken, from radio occultation electron density profiles on board low Earth orbit (LEO) satellites from the COSMIC/FORMOSAT-3 mission, in the vicinity of digisonde stations on a global scale. A subset of these radio occultation profiles, with matched (within 5%) peak NmF2 and hmF2 characteristics is also exploited to focus the comparison to a high quality validation dataset. The comparison shows that α-Chapman and Corrected NeQuick underestimate, whereas IRI-NeQuick overestimates COSMIC topside electron density observations. The key parameter g which controls the change of scale height w.r.t. altitude near the F region peak is optimised to a value of 0.15 (compared to a currently adopted value of 0.125). The Corrected NeQuick topside formulation using the optimised g value of 0.15 (represented as New_g) outperforms all other topside formulations.

1. Introduction

The COSMIC/FORMOSAT-3 (Constellation Observing System for Meteorology, Ionosphere, and Climate and Formosa Satellite) mission has been very successful in facilitating the vertical profiling of the atmosphere and the study of the topside ionosphere (Anthes R.A. et al., 2008). The radio occultation (RO) technique is based on precise dual-frequency phase measurements (Schreiner et al., 1999) from GNSS receivers on board Low-Earth Orbit (LEO) satellites that exploit radio signals transmitted from global navigation satellite system (GNSS) satellites. Many authors have worked on the validation of COSMIC data using co-located digisonde and Incoherent Scatter Radar (ISR) stations (Stankov and Jakowski, 2006; Lei et al., 2007; Krankowski et al., 2011; Yue et al., 2011; Cherniak and Zakharenkova, 2014; Hu et al., 2014; McNamara and Thompson, 2015; Panda et al., 2018; Shaikh et al., 2018; Wang et al., 2019; Bai et al., 2019).

The topside part of the ionosphere is defined as the region between the maximum electron density of the F2 layer to the upper transition height (Rishbeth and Garriott, 1969). The transition of heavy O^+ ions to lighter H^+ ions leads to a smooth decrease in the electron

density. This smooth decrease is expressed by a parameter called scale height (Hargreaves, 1992). To determine the scale height, the information of the mean ion mass, their chemical state and plasma temperature must be known but this information is not available on a global scale. So there are alternative methods to estimate the effective scale height based on electron density measurements (Liu et al., 2007a, 2007b) since to accurately model the topside ionosphere, the effective scale height is a major requirement.

The International Ionosphere Model (IRI) -2016 (Bilitiza et al., 2017) offers three options to model the electron density in the topside ionosphere, IRI-2001 (Bilitiza, 1990), IRI01-corr (Bilitiza, 2004) and the most reliable NeQuick (Radicella and Leitinger, 2001; Coisson et al., 2006; Nava et al., 2008) but according to past and recent studies there is still room for improvement (Bilitiza et al., 2006, Bilitiza, 2009; Pignalberi et al., 2016). The NeQuick topside model uses an Epstein function (as shown in equation 1) to model the topside ionosphere. The electron density profile (Ne (h)) is constructed as a function of *hm*F2, *Nm*F2 and effective scale height (Hm).

$$\text{Ne (h)} = 4.NmF2.\ \frac{exp\left(\frac{h-hmF2}{Hm}\right)}{\left(1+exp\left(\frac{h-hmF2}{Hm}\right)\right)^2} \quad (1)$$

$$\text{Hm} = H_0\left[1+\frac{r\cdot g(h-hmF2)}{r\cdot H_0+g\cdot(h-hmF2)}\right] \quad (2)$$

The scale height in the NeQuick topside formulation is described by three parameters, scale height at the peak (H_0), parameter r which restricts the scale height at higher altitudes and the altitude gradient of the scale height (g). A value of r =100 and g =0.125 is adopted in NeQuick topside formulation, while H_0 is estimated from equation (3), where *fo*F2 is the peak critical frequency, *Nm*F2 is the peak electron density, *hm*F2 is the height corresponding to *Nm*F2 and R12 is the 12 month smoothed sunspot number.

$$H_0 = k.B2_{Bot} \quad (3)$$

$$k = 3.22 - 0.0538 * foF2 - 0.00664 * hmF2 + 0.113 * \frac{hmF2}{B2_{Bot}} + 0.00257 * R12 \quad (4)$$

An improvement in the NeQuick topside formulation (NeQuick-corr [Pezzopane and Pignalberi, 2019]) has been recently proposed. This Corrected NeQuick topside formulation is based on H_0 grids, as a function of *hm*F2 and *Nm*F2, generated by applying the IRI-UP (Update) method (Pignalberi et al., 2018) and also by exploiting electron density values measured by the Langmuir probes on-board Swarm satellites. According to this method, H_0 is

estimated as $H_{0,\,AC}$ and $H_{0,\,B}$ at two different altitudes for each pair of *hm*F2 and *Nm*F2 values to determine a new H_0 formulation in accordance to equations (45) and (6).

$$H_0 = H_{0,\,AC} + (H_{0,\,B} - H_{0,\,AC}) \cdot \frac{h - hmF2}{600} \qquad \text{for } hmF2 \le h < hmF2+600 \tag{5}$$

$$H_0 = H_{0,\,B} \qquad \text{for } h \ge hmF2+600 \tag{6}$$

where two 2-D grids provide the values of $H_{0,\,AC}$ and $H_{0,\,B}$ as a function of *fo*F2 and *hm*F2.

Themens et al., 2018 demonstrated that the IRI-NeQuick option can be improved over upper mid latitude and high latitude regions by adjusting r and g values to r =20 and g = 0.2024. Another study by Themens et al., 2014 showed that IRI-NeQuick parameterization does not adequately represent the topside thickness during solar minimum between cycles 23 and 24 and Pignalberi et al., 2020 underlined the significance of r and g in the topside scale height variation near the F2-layer peak (up to about 800 km). They have shown that the topside scale height exhibits a linear dependence on the peak-relative altitude (h-*hm*F2), where g is the slope and H_0 is the intercept, as follows:

$$H(h) \simeq H_0 + g \times (h - hmF2) \tag{7}$$

In view of the above, in this paper, topside electron density values retrieved from 29063 COSMIC RO profiles in the vicinity of 44 digisonde stations are compared with α-Chapman, IRI-NeQuick, and Corrected-NeQuick topside model electron density estimates. Furthermore, we show that a new g value of 0.15 produces better results using Corrected-NeQuick. To validate this new g value in the Corrected-NeQuick topside formulation, scale height has been deduced from each COSMIC RO based on the valid assumption (up to 800 km) of a linear dependence with altitude. This could be significant, in the context of the single-frequency GNSS correction algorithm (NeQuick-G) adopted by European Space Agency (ESA) Galileo GNSS system, as r=100 and g=0.125 are the values embedded in the existing version of NeQuick-G.

2. Data

The comparison between topside COSMIC RO profiles (downloaded from the CDAAC data server https://cdaac-www.cosmic.ucar.edu/cdaac/products.html) and digisonde topside profiles was carried out under time and space coincidence requirements. In particular the COSMIC topside electron density value considered, was the one at a minimum distance to the digisonde location (as shown in Figure 1). Figure 1 shows the COSMIC RO profile with respect to latitude and longitude, where the red part of the profile shows the bottomside

projection and blue part shows the topside profile projection. It also shows the nearest digisonde station (Nicosia station as an example) and the minimum (perpendicular) distance between digisonde station and topside profile. We have also excluded any unrealistic RO profiles with excessive fluctuations in the topside electron density and hmF2 outside the range [150<hmF2<450] km. In total 29063 profiles in the interval 2006-2018 were considered. The autoscaled digisonde data were downloaded from the Digital Ionogram Data Base (DIDBase- http://giro.uml.edu/didbase/scaled.php). The selected digisonde stations, their location (latitude, longitude) and the number of nearest selected COSMIC profiles are shown in Table 1. To construct the digisonde topside electron density profile, *hm*F2, *fo*F2 and scale height values were applied in α-Chapman function, shown in equation (8):

$$\text{Ne (h)} = NmF2.exp\left\{\frac{1}{2}\left[1-\frac{h-hmF2}{H}exp\left(-\frac{h-hmF2}{H}\right)\right]\right\} \quad (8)$$

The corresponding IRI-NeQuick values were also estimated at the corresponding COSMIC topside electron density altitude (at a minimum distance from the corresponding digisonde) using the FORTRAN source code for IRI 2016, available at http://irimodel.org/ by ingesting *hm*F2 and *fo*F2 auto-scaled values. The Corrected-NeQuick values were estimated by calculating H_0 using the $H_{0,AC}$ and $H_{0,B}$ grid (downloaded from the supplementary data of the Pezzopane and Pignalberi, (2019)) for the same *hm*F2 and *Nm*F2 values. This dataset is termed as DATABSE 1. To compare COSMIC to α-Chapman (digisonde), IRI-NeQuick, Corrected NeQuick and New_g Corrected NeQuick data, relative differences were calculated as shown below:

$$\text{Relative difference } (RD_{CD}) = \frac{\text{COSMIC electron density} - \text{digisonde electron density}}{\text{COSMIC electron density}} \quad (9)$$

$$\text{Relative difference } (RD_{CIRI}) = \frac{\text{COSMIC electron density} - \text{IRI-NeQuick model electron density}}{\text{COSMIC electron density}} \quad (10)$$

$$\text{Relative difference } (RD_{CCN}) = \frac{\text{COSMIC electron density} - \text{Corrected NeQuick model electron density}}{\text{COSMIC electron density}} \quad (11)$$

$$\text{Relative difference } (RD_{CICN}) = \frac{\text{COSMIC electron density} - New_g \text{Corrected NeQuick model electron density}}{\text{COSMIC electron density}}$$

(12)

The second dataset used in this investigation is based on a subset of DATASET 1 for which coincidence at the peak values (*Nm*F2, *hm*F2) of the profile within <5% difference in *hm*F2 and *Nm*F2 was satisfied, in an effort to ensure more reliable topside profiles in accordance to findings in a previous study (Shaikh et al., 2018). We have found thirty four hundred thirty three (3433) such cases out of 29,063 cases from DATASET 1, based on which, we have calculated corresponding IRI-NeQuick, Corrected NeQuick and New_g Corrected profiles. This dataset is termed as DATASET 2.

To compare the full topside profiles recorded by the COSMIC RO satellites and modeled by α-Chapman (digisonde), IRI-NeQuick, Corrected NeQuick and New_g Corrected NeQuick a relative difference (as a function of altitude beyond the peak) was calculated as shown below:

$$\text{Relative difference } (RD_{CD}(h)) = \frac{\text{COSMIC electron density (h)} - \text{digisonde electron density(h)}}{\text{COSMIC electron density (h)}}$$

(13)

$$\text{Relative difference } (RD_{CIRI}(h)) = \frac{\text{COSMIC electron density (h)} - \text{IRI-NeQuick model electron density(h)}}{\text{COSMIC electron density (h)}}$$

(14)

$$\text{Relative difference } (RD_{CCN}(h)) = \frac{\text{COSMIC electron density(h)} - \text{Corrected NeQuick electron density(h)}}{\text{COSMIC electron density(h)}}$$

(15)

$$\text{Relative difference } (RD_{CICN}(h)) = \frac{\text{COSMIC electron density (h)} - New_g\text{Corrected NeQuick model electron density (h)}}{\text{COSMIC electron density (h)}}$$

(16)

and,

$$htop = h - hmF2 \quad (17)$$

htop denotes the peak-relative altitude in km.

To investigate the overall performance in terms of the full profile in the various topside formulations, a Normalised Root Mean Square Error (NRMSE) was calculated for each of the 3433 profiles for DATASET 2, using:

$$\text{NRMSE} = \sqrt{\frac{\sum_{i=1}^{N}\left(\frac{Ne_{measured,i} - Ne_{modeled,i}}{Ne_{measured,i}}\right)^2}{N}} \quad (18)$$

where subscript *measured* refers to COSMIC measurements, while *modeled* to either α-Chapman, IRI-NeQuick or Corrected NeQuick. *N* is the total number of electron density profile points.

The scale height (Hm) was calculated for COSMIC, α-Chapman, IRI-NeQuick and Corrected NeQuick data from the Epstein equation as shown below. Pignalberi et al., (2020) also have used same approach to calculate scale height from COSMIC profile.

$$\text{N (h)} = 4.Nm\text{F2}.\ \frac{exp\left(\frac{h-hmF2}{Hm}\right)}{\left(1+exp\left(\frac{h-hmF2}{Hm}\right)\right)^2} \quad (19)$$

$$\frac{N\ (h)}{4NmF2} = \frac{exp\left(\frac{h-hmF2}{Hm}\right)}{\left(1+exp\left(\frac{h-hmF2}{Hm}\right)\right)^2}$$

Let,

$$\text{Y} = exp\left(\frac{h-hmF2}{Hm}\right) \quad (20)$$

$$\text{X} = \frac{N\ (h)}{4NmF2} \quad (21)$$

then the equation becomes:

$$\text{X (1+Y)}^2 = \text{Y}$$

$$\text{X Y}^2 + (2\text{X-1})\ \text{Y} + \text{X} = 0 \quad (22)$$

By using the Sridhar Acharya formula, the solution for the above quadratic equation reduces to:

$$\text{Y (1, 2)} = \frac{\left[(2\text{NmF2} - \text{N(h)}) \pm 2\sqrt{NmF2^2 - N(h).NmF2}\right]}{N(h)} \quad (23)$$

and by solving equation (19) and (23), Hm would be:

$$\text{Hm} = \frac{h-hmF2}{\ln Y(1,2)} \quad (24)$$

The calculated scale height from equation 24 was used to check the linear fit dependence.

3. Results:

The comparison between topside electron density profile measurements and model formulations, as described in section 2 is presented in the following sections. The results in section (3.1) are based on DATASET 1 and section (3.2) and (3.3) are based on DATASET 2.

3.1 Comparison based on DATASET 1

Figure 2 (a) shows the binned scatter plot between peak-relative altitude (htop=h-*hm*F2) and relative difference (RD_{CD}) between COSMIC observations and α-Chapman estimations, while the colour bar shows the counts in each bin. As it can be seen from the graph, in the vast majority of cases RD_{CD} is greater than zero which indicates that α-Chapman underestimates COSMIC observations and this difference increases with htop with the bin occurrence maximising around 500 km (above *hm*F2). The findings from Figure 2 (a) are justified because digisonde topside estimation is based on a α-Chapman function, with a constant scale height (as shown in Figure 2 (b)), but real observations differ from α-Chapman estimates because scale height increases linearly with height over the peak (Olivares-Pulido et al., 2016). The scale height behaviour of COSMIC observations (as shown in Figure 5) was calculated from DATASET 1 using equation 24.

Figure 3(a) shows the binned scatter plot between peak-relative altitude (htop) and relative difference (RD_{CIRI}) between COSMIC observations and IRI-NeQuick estimates. It shows that IRI-NeQuick slightly overestimates the COSMIC observations up to an approximate htop altitude of 300km and then its behaviour reverses underestimating COSMIC measurements. IRI-NeQuick is based on an Epstein function to represent the topside profile with an approximately linear scale height (calculated using equation 24, as shown in Figure 3 (b)) and therefore its performance is superior to α-Chapman. The IRI-NeQuick considers values of r=100 and g=0.125 for calculating the scale height. The error with respect to htop as shown in Figure 3 (a) could be due to the difference in the change of scale height with w.r.t. htop (g) between COSMIC observations and IRI-NeQuick estimations (Themens et al., 2018).

Figure 4 (a) shows the binned scatter plot between peak-relative altitude (htop) and relative difference (RD_{CCN}) between COSMIC observations and Corrected NeQuick estimates. It shows that Corrected NeQuick underestimates COSMIC observations and this underestimation increases with htop. The Corrected NeQuick is equivalent to IRI-NeQuick but the value of H_0 is deduced from $H_{0,AC}$ and $H_{0,B}$ grids and the scale height (as shown in

Figure 4 (b)) is calculated by equation 24 following equations 5 and 6 as proposed by Pezzopane and Pignalberi, (2019). As it is clear from Figure 3 (a) and Figure 4 (a), for the majority of cases IRI-NeQuick exhibits an approximate error in the range -0.2 to 0.4 and for Corrected NeQuick the error lies in the range of 0 to 0.35 respectively, which demonstrates that Corrected NeQuick outperforms IRI-NeQuick.

The above results clearly indicate that the scale height calculated using different H_0 formulations is not able to match the scale height calculated from COSMIC observations and that further potential improvement could be achieved by more appropriate values for r and g (Themens et al., 2018). To explore this possibility, we used least squares to optimize the value of g and r keeping H_0 constant for Corrected NeQuick. The value of r varied with a step size of 1 and g with a step size of 0.01. As the COSMIC data were mostly limited to an altitude below 800 km, since r controls the scale height at higher altitudes, r did not change at all during this optimization (r=100). Pignalberi et al., (2020) also showed that the effect of varying r on the scale height, is seen on the altitude much higher from the F2 peak. Figure 6 shows the variation of r and g with respect to the RMSE calculated between COSMIC observations and Corrected-NeQuick estimates. COSMIC and Corrected NeQuick comparison showed that for r =100 and an optimised value of g = 0.15, RMSE minimizes. In this method, to estimate the electron density, the Epstein equation was used and scale height was calculated using H_0 extracted from the $H_{0,AC}$ and $H_{0,B}$ grid r =100 and g = 0.15. Figure 7 (a) shows the binned scatter plot between peak-relative altitude and relative difference (RD_{CICN}) between COSMIC observations and New_g Corrected NeQuick estimates. It shows that the $RD_{(CICN)}$ is almost constant with htop and it is confined within a bounded region. So by comparing all four methods (Figure 2, 3, 4&7) it can be stated that the performance of New_g Corrected NeQuick method is better than the other four methods for this particular dataset. The scale height (calculated from equation 24 for New_g Corrected NeQuick method is shown in Figure 7 (b).

3.2 Comparison based on DATASET 2

DATASET 2 is a subset of DATASET 1 comprising of 3433 matched peak profiles (within <5% difference in *hm*F2 and *Nm*F2). Figure 8 (a) and (b) show the binned scatter plot between peak-relative altitude (htop=h-*hm*F2) and relative difference (RD_{CD} (h)) between COSMIC and α-Chapman profiles, for h-*hm*F2>100 and h-*hm*F2<100 respectively. The colour bar represents the counts in each bin. As discussed in section (3.1), α-Chapman

underestimates COSMIC observations and it increases with htop, which can also be observed from Figure 8(a) as RD_{CD} (h) increases with htop. Figure 8 (b) shows that up to 100 km over *hm*F2, the average RD_{CD} (h) fluctuates around zero. This is expected as α-Chapman scale height is constant, around the peak.

Figure 9 (a) and (b) show scatter plots between peak-relative altitude (htop) and relative difference (RD_{CIRI} (h)) between COSMIC profile and IRI-NeQuick estimated profile, for h-*hm*F2>100 and h-*hm*F2<100 respectively. Figure 9 (a) shows that IRI-NeQuick overestimates (-0.5 to 0 for the majority of profiles) COSMIC up to approximately htop=300km and then its behaviour reverses with a definite underestimation (within 0 to 0.2 for most profiles). The results are similar with the findings discussed in section (3.1) indicating that IRI-NeQuick clearly outperforms α-Chapman. Figure 9 (b) shows that up to htop =100km, the average RD_{CIRI} (h) fluctuates around 0, which suggests that IRI-NeQuick also exhibits approximately constant scale height around the peak.

Figure 10 (a) and (b) shows the binned scatter plot between peak-relative altitude (htop) and relative difference (RD_{CCN} (h)) between COSMIC and Corrected NeQuick, for h-*hm*F2>100 km and h-*hm*F2<100 km respectively. Figure 10 (a) shows that Corrected NeQuick underestimates COSMIC and RD_{CCN} (h) increases (0 to 0.5) with htop. Unlike IRI-NeQuick, the behaviour of Corrected NeQuick does not reverse with htop, whereas the RD_{CCN} (h) gets saturated for htop >300km. Figure 10 (b) shows that up to htop =100km average RD_{CCN} (h) fluctuates around zero suggesting that like α-Chapman and IRI-NeQuick, Corrected NeQuick also exhibits nearly constant scale height around the peak.

NRMSE between COSMIC and the three topside formulations was also calculated. Figure 11 (a) shows the scatter plot between the NRMSE values for Corrected NeQuick (w.r.t. COSMIC) on x axis and NRMSE values for α-Chapman (w.r.t. COSMIC) on y axis. For the majority of cases NRMSE-α-Chapman exceeds NRMSE-Corrected NeQuick, which means Corrected NeQuick performs better than α-Chapman. Figure 11 (b) shows the scatter plot between NRMSE-Corrected NeQuick (w.r.t. COSMIC) on x axis and NRMSE-IRI-NeQuick (w.r.t. COSMIC) on y axis for each individual matched peak profile. It shows that NRMSE-Corrected NeQuick is lower for nearly half the cases (1803 out of 3433) and NRMSE-IRI-NeQuick is lower for the rest (1640 out of 3433) but for the majority NRMSE-Corrected NeQuick is more bounded (from 0 to 0.5) whereas NRMSE-IRI-NeQuick extends from 0 up to 0.8. Therefore, we can conclude that Corrected-NeQuick is superior to IRI-NeQuick for

representing the topside, based on the particular COSMIC dataset under consideration. Klipp et al., (2020) recently applied the Corrected NeQuick method to study the comparison between the ionospheric total electron content from ionosondes and the International GNSS service vertical total electron content and reported that the error was reduced by 27 %.

The values of r = 100 and optimised value of g = 0.15 for Corrected NeQuick on DATASET 1 in section (3.1) were also tested for DATASET 2. Figure 12 (a) and (b) show the binned scatter plot between peak-relative altitude (htop) and relative difference (RD_{CICN} (h)) between COSMIC and Corrected NeQuick, for h-*hm*F2>100 and for h-*hm*F2<100. Figure 12 (a) clearly shows that the RD_{CICN} (h) is almost constant with respect to htop and that it is confined within a region (-0.2 to 0.2). RD_{CICN} (h) is also almost 0 for h-*hm*F2<100, as shown in Figure 12 (b). By comparing Figure 8, 9, 10 and12, it is clear that Corrected-NeQuick with a value of g=0.15 outperforms all other topside formulations for DATASET 2 as well.

3.3 Topside scale height linear variation and validation of optimised value of g = 0.15 using DATASET 2.

As discussed in section (3.1) and (3.2), the behaviour of the topside scale height is expected to be linear. So to verify this for all matched peak COSMIC profiles (3433 profiles in DATASET 2), the scale height was calculated using equation 24. The scale height of each profile was fitted under a linear approximation as shown in Figure 13 (a) and subsequently the corresponding electron density profiles were calculated. Figure 13 (b) shows the relative difference between measured and modeled electron density (using linearly fitted scale height). Figure 13 (b) clearly shows that most of the error lies within 5%. This verifies the linear scale height variation up to 500 km over *hm*F2 (Pignalberi et al., 2020). The value of g was also calculated for each of the linear fitted scale height matched peak COSMIC profiles using equation 7. The results are in line with those obtained by Pignalberi et al., (2020).

Figure 14 shows the variation of g (calculated from equation 7) with respect to RMSE between COSMIC and linearly fitted scale-height electron density profiles from DATASET 2. It shows that for the majority of the profiles, a value of g = 0.15 (±0.015) minimises RMSE. As it was discussed in section (3.1) and (3.2), for an optimum value of g = 0.15, Relative difference between COSMIC and Corrected NeQuick minimises and exhibits the best performance among all four topside formulations tested on both DATASET 1 and 2.

4. Conclusion:

A comparison study between COSMIC topside electron density observations and α-Chapman, IRI-NeQuick and Corrected NeQuick estimations has resulted in the following conclusions:

1) The overall performance of Corrected NeQuick is superior to IRI-NeQuick, as the NRMSE introduced by the former is confined (from 0 to 0.5) than the latter (from 0 to 0.8) for the vast majority of cases.
2) For an optimum value of g = 0.15, New_g Corrected NeQuick performance improves further. This could be significant, in the context of the single-frequency GNSS correction algorithm (NeQuick-G) adopted by European Space Agency (ESA) Galileo GNSS system, as r=100 and g=0.125 are the values embedded in the existing version of NeQuick-G.
3) Electron density profiles derived from a linear fitted scale height as extracted from COSMIC electron density profiles lie within 5% relative difference.
4) The best linear fit scale height shows that for the optimised value of g = 0.15, RMSE is lowest between COSMIC and linearly fitted scale-height electron density profiles

Acknowledgement:

This study was funded by the project “Service for Improving Galileo operation over Cyprus” (SERVING)-ENTERPRISES/0916/0159 which is co-funded by the Republic of Cyprus and the European Regional Development Fund (through the 'RESEARCH IN ENTERPRISES' RESTART 2016-2020 Programme for Research, Technological Development and Innovation). The authors would like to thank, CDAAC team (COSMIC Data Analysis and Archive Centre) for the COSMIC/FORMOSAT-3 for making data publicly available via their website (https://cdaac-www.cosmic.ucar.edu/cdaac/products.html). The authors would like to thank the IRI team for sharing the IRI Model code (http://irimodel.org/). The author would also like to thank Michael Pezzopane and Alessio Pignalberi from the Istituto Nazionale di Geofisica e Vulcanologia, Italy, for providing access to median values of $H_{0,AC}$ and $H_{0,B}$ as a function of *fo*F2 and *hm*F2 (Pezzopane & Pignalberi, 2019).

References:

1. Anthes, R. A., Bernhardt, P. A., Chen, Y., Cucurull, L., Dymond, K. F., Ector, D., Healy, S. B., Ho, S.-P., Hunt, D. C., Kuo, Y.-H., Liu, H., Manning, K., McCormick, C., Meehan, T. K., Randel, W. J., Rocken, C., Schreiner, W. S., Sokolovskiy, S. V., Syndergaard, S., Thompson, D. C., Trenberth, K. E., Wee, T.-K., Yen, N. L., and Zeng, Z. (2008).“The COSMIC/FORMOSAT-3 Mission: Early Results”. Bull. Amer. Meteor. Soc., 89, 313–333. https://doi.org/10.1175/BAMS-89-3-313.
2. Lei, J., Syndergaard, S., Burns, A. G., Solomon, S. C., Wang, W., Zeng, Z., & Zhang, S. R. (2007). Comparison of COSMIC ionospheric measurements with ground-based observations and model predictions: Preliminary results. Journal of Geophysical Research: Space Physics, 112(A7). https://doi.org/10.1029/2006JA012240.
3. Krankowski, A., Zakharenkova, I., Krypiak-Gregorczyk, A., Shagimuratov, I. I., & Wielgosz, P. (2011). Ionospheric electron density observed by FORMOSAT-3/COSMIC over the European region and validated by ionosonde data. Journal of Geodesy, 85(12), 949-964. https://doi.org/10.1007/s00190-011-0481-z.
4. Yue, X., Schreiner, W. S., Hunt, D. C., Rocken, C., & Kuo, Y. H. (2011). Quantitative evaluation of the low Earth orbit satellite based slant total electron content determination. Space Weather, 9(9). https://doi.org/10.1029/2011SW000687.
5. Cherniak, I. V., & Zakharenkova, I. E. (2014). Validation of FORMOSAT-3/COSMIC radio occultation electron density profiles by incoherent scatter radar data. Advances in Space Research, 53(9), 1304-1312. https://doi.org/10.1016/j.asr.2014.02.010.
6. Hu, L., Ning, B., Liu, L., Zhao, B., Li, G., Wu, B., & Wu, Z. (2014, October). Validation of COSMIC ionospheric peak parameters by the measurements of an ionosonde chain in China. In Annales Geophysicae (Vol. 32, No. 10, pp. 1311-1319). Copernicus GmbH. https://doi.org/10.5194/angeo-32-1311-2014.
7. McNamara, L. F., & Thompson, D. C. (2015). Validation of COSMIC values of foF2 and M (3000) F2 using ground-based ionosondes. Advances in Space Research, 55(1), 163-169. https://doi.org/10.1016/j.asr.2014.07.015.
8. Panda, S. K., Haralambous, H., & Kavutarapu, V. (2018). Global Longitudinal Behavior of IRI Bottomside Profile Parameters From FORMOSAT-3/COSMIC

Ionospheric Occultations. Journal of Geophysical Research: Space Physics, 123(8), 7011-7028. https://doi.org/10.1029/2018JA025246.

9. Shaikh, M. M., Nava, B., & Haralambous, H. (2018). On the Use of Topside RO-Derived Electron Density for Model Validation. Journal of Geophysical Research: Space Physics, 123(5), 3943-3954. https://doi.org/10.1029/2017JA025132.
10. Wang, X., Cheng, W., Zhou, Z., Xu, S., Yang, D., & Cui, J. (2019, November). Comparison of CSES ionospheric RO data with COSMIC measurements. In Annales Geophysicae (Vol. 37, No. 6, pp. 1025-1038). Copernicus GmbH). https://doi.org/10.5194/angeo-37-1025-2019.
11. Bai, W., Tan, G., Sun, Y., Xia, J., Cheng, C., Du, Q., …& Meng, X. (2019). Comparison and validation of the ionospheric climatological morphology of FY3C/GNOS with COSMIC during the recent low solar activity period. Remote Sensing, 11(22), 2686. https://doi.org/10.3390/rs11222686.
12. Rishbeth, H., & Garriott, O. K. (1969). Introduction to ionospheric physics (Vol. 14). New York: Academic Press.
13. Hargreaves, J. K. (1992). The solar-terrestrial environment: an introduction to geospace-the science of the terrestrial upper atmosphere, ionosphere, and magnetosphere. Cambridge university press.
14. Liu, L., Le, H., Wan, W., Sulzer, M. P., Lei, J., & Zhang, M. L. (2007a). An analysis of the scale heights in the lower topside ionosphere based on the Arecibo incoherent scatter radar measurements. Journal of Geophysical Research: Space Physics, 112(A6). https://doi.org/10.1029/2007JA012250.
15. Liu, L., Wan, W., Zhang, M. L., Ning, B., Zhang, S. R., & Holt, J. M. (2007b). Variations of topside ionospheric scale heights over Millstone Hill during the 30-day incoherent scatter radar experiment. https://hal.archives-ouvertes.fr/hal-00318384.
16. Bilitza, D., Altadill, D., Truhlik, V., Shubin, V., Galkin, I., Reinisch, B., & Huang, X. (2017). International Reference Ionosphere 2016: From ionospheric climate to real-time weather predictions. Space Weather, 15(2), 418-429. https://doi.org/10.1002/2016SW001593.
17. Bilitza, D. (1990). International Reference Ionosphere 1990, National Space Science Data Center. NSSDC/WDC-AR &S 90-22.
18. Bilitza, D. (2004). A correction for the IRI topside electron density model based on Alouette/ISIS topside sounder data. Advances in Space Research, 33(6), 838-843. https://doi.org/10.1016/j.asr.2003.07.009.

19. Radicella, S. M., & Leitinger, R. (2001). The evolution of the DGR approach to model electron density profiles. Advances in Space Research, 27(1), 35-40. https://doi.org/10.1016/S0273-1177(00)00138-1.
20. Coïsson, P., Radicella, S. M., Leitinger, R., & Nava, B. (2006). Topside electron density in IRI and NeQuick: Features and limitations. Advances in Space Research, 37(5), 937-942. https://doi.org/10.1016/j.asr.2005.09.015.
21. Nava, B., Coisson, P., & Radicella, S. M. (2008). A new version of the NeQuick ionosphere electron density model. Journal of Atmospheric and Solar-Terrestrial Physics, 70(15), 1856-1862. https://doi.org/10.1016/j.jastp.2008.01.015.
22. Bilitza, D. (2009). Evaluation of the IRI-2007 model options for the topside electron density. Advances in space research, 44(6), 701-706. https://doi.org/10.1016/j.asr.2009.04.036.
23. Bilitza, D., Reinisch, B. W., Radicella, S. M., Pulinets, S., Gulyaeva, T., & Triskova, L. (2006). Improvements of the International Reference Ionosphere model for the topside electron density profile. Radio science, 41(05), 1-8. https://doi.org/10.1029/2005RS003370.
24. Pignalberi, A., Pezzopane, M., Tozzi, R., De Michelis, P., & Coco, I. (2016). Comparison between IRI and preliminary Swarm Langmuir probe measurements during the St. Patrick storm period. Earth, Planets and Space, 68(1), 93. https://doi.org/10.1186/s40623-016-0466-5.
25. Pezzopane, M., & Pignalberi, A. (2019). The ESA Swarm mission to help ionospheric modeling: a new NeQuick topside formulation for mid-latitude regions. Scientific reports, 9(1), 1-12. https://doi.org/10.1038/s41598-019-48440-6.
26. Pignalberi, A., Pietrella, M., Pezzopane, M., & Rizzi, R. (2018). Improvements and validation of the IRI UP method under moderate, strong, and severe geomagnetic storms. Earth, Planets and Space, 70(1), 180. https://doi.org/10.1186/s40623-018-0952-z.
27. Schreiner, W.S., Sokolovskiy, S.V., Rocken, C. and Hunt, D.C. (1999). Analysis and validation of GPS/MET radio occultation data in the ionosphere. Radio Science, 34(4), pp.949-966. https://doi.org/10.1029/1999RS900034.
28. Stankov, S. M., & Jakowski, N. (2006). Topside ionospheric scale height analysis and modelling based on radio occultation measurements. Journal of atmospheric and solar-terrestrial physics, 68(2), 134-162. https://doi.org/10.1016/j.jastp.2005.10.003.

29. Themens, D. R., Jayachandran, P. T., Bilitza, D., Erickson, P. J., Häggström, I., Lyashenko, M. V., & Pustovalova, L. (2018). Topside electron density representations for middle and high latitudes: A topside parameterization for E-CHAIM based on the NeQuick. Journal of Geophysical Research: Space Physics, 123(2), 1603-1617. https://doi.org/10.1002/2017JA024817.
30. Themens, D. R., Jayachandran, P. T., Nicolls, M. J., & MacDougall, J. W. (2014). A top to bottom evaluation of IRI 2007 within the polar cap. Journal of Geophysical Research: Space Physics, 119(8), 6689-6703. https://doi.org/10.1002/2014JA020052.
31. Pignalberi, A., Pezzopane, M., Themens, D. R., Haralambous, H., Nava, B., & Coïsson, P. (2020). On the Analytical Description of the Topside Ionosphere by NeQuick: Modeling the Scale Height Through COSMIC/FORMOSAT-3 Selected Data. IEEE Journal of Selected Topics in Applied Earth Observations and Remote Sensing, 13, 1867-1878. 10.1109/JSTARS.2020.2986683.
32. Olivares-Pulido, G., Hernández-Pajares, M., Aragón-Àngel, A., & Garcia-Rigo, A. (2016). A linear scale height Chapman model supported by GNSS occultation measurements. Journal of Geophysical Research: Space Physics, 121(8), 7932-7940. https://doi.org/10.1002/2016JA022337.
33. Klipp, T. D. S., Petry, A., Souza, J. R. D., Paula, E. R. D., Falcão, G. S., & Campos Velho, H. F. D. (2020, March). Ionosonde total electron content evaluation using International Global Navigation Satellite System Service data. In Annales Geophysicae (Vol. 38, No. 2, pp. 347-357). Copernicus GmbH. https://doi.org/10.5194/angeo-38-347-2020.

Table captions:

Table 1: The Ionosonde stations name (Country) collocated with the COSMIC RO profiles with their location (geographic latitude, longitude), geomagnetic latitude, Number of coincident observations and Number of Matched Peak Profiles.

Figure Caption:

Figure 1: The graph shows the COSMIC RO profile variation with respect to Latitude (on y axis) and Longitude (on x-axis) and Nearest Digisonde station which meets the topside coincident criteria.

Figure 2: The graph shows the binscatter plot of (a) Relative difference (RD_{CD}) between COSMIC observations and α-Chapman estimations (b) Scale height of α-Chapman estimations as a function of peak-relative altitude (h-*hm*F2).

Figure 3: The graph shows the binscatter plot of (a) Relative difference (RD_{CIRI}) between COSMIC observations and IRI-NeQuick estimations (b) Scale height of IRI-NeQuick estimations as a function of peak-relative altitude (h-*hm*F2).

Figure 4: The graph shows the binscatter plot of (a) Relative difference (RD_{CCN}) between COSMIC observations and Corrected NeQuick estimations (b) Scale height of Corrected NeQuick estimations as a function of peak-relative altitude (h-*hm*F2).

Figure 5: The graph shows the binscatter plot of Scale height of COSMIC observations as a function of peak-Relative altitude (h-*hm*F2).

Figure 6: The graph shows the contour plot of RMSE between COSMIC observations and Corrected NeQuick estimations for varying value of r and g.

Figure 7: The graph shows the binscatter plot of (a) Relative difference (RD_{CICN}) between COSMIC observations and New_g Corrected estimations (b) Scale height of New_g Corrected estimations as a function of peak-relative altitude (h-*hm*F2).

Figure 8: The graph shows the binscatter plot of relative difference (RD_{CD} (h)) between COSMIC observed and α-Chapman estimated matched peak electron density profiles for (a) h-*hm*F2>100 (b) h-*hm*F2<100 as a function of peak-relative altitude (h-*hm*F2).

Figure 9: The graph shows the binscatter plot of relative difference (RD_{CIRI} (h)) between COSMIC observed and IRI-NeQuick estimated matched peak electron density profiles for (a) h-*hm*F2>100 (b) h-*hm*F2<100 as a function of peak-relative altitude (h-*hm*F2).

Figure 10: The graph shows the binscatter plot of relative difference (RD_{CCN} (h)) between COSMIC observed and Corrected NeQuick estimated matched peak electron density profiles for (a) h-*hm*F2>100 (b) h-*hm*F2<100 as a function of peak-relative altitude (h-*hm*F2).

Figure 11: The graph shows the scatter plot between the NRMSE_Corrected NeQuick (a) NRMSE_ α-Chapman (b) NRMSE_IRI-NeQuick for matched peak profiles. The Red line shows the y=x line on the graph.

Figure 12: The graph shows the binscatter plot of relative difference (RD_{CICN} (h)) between COSMIC observed and New_g Corrected NeQuick estimated matched peak electron density profiles for (a) h-*hm*F2>100 (b) h-*hm*F2<100 as a function of peak-relative altitude (h-*hm*F2).

Figure 13: The graph shows the (a) variation of Scale height inverted from COSMIC profile (blue dots) and red line shows the best linear fit line (b) Relative difference between the COSMIC matched peak profiles and corresponding linear fitted profiles as a function of peak-relative altitude (h-*hm*F2).

Figure 14: The graph shows the RMSE between the COSMIC matched peak profiles and corresponding linear fitted profiles with respect to the slope of best linear fit line (g).

Figure 1.

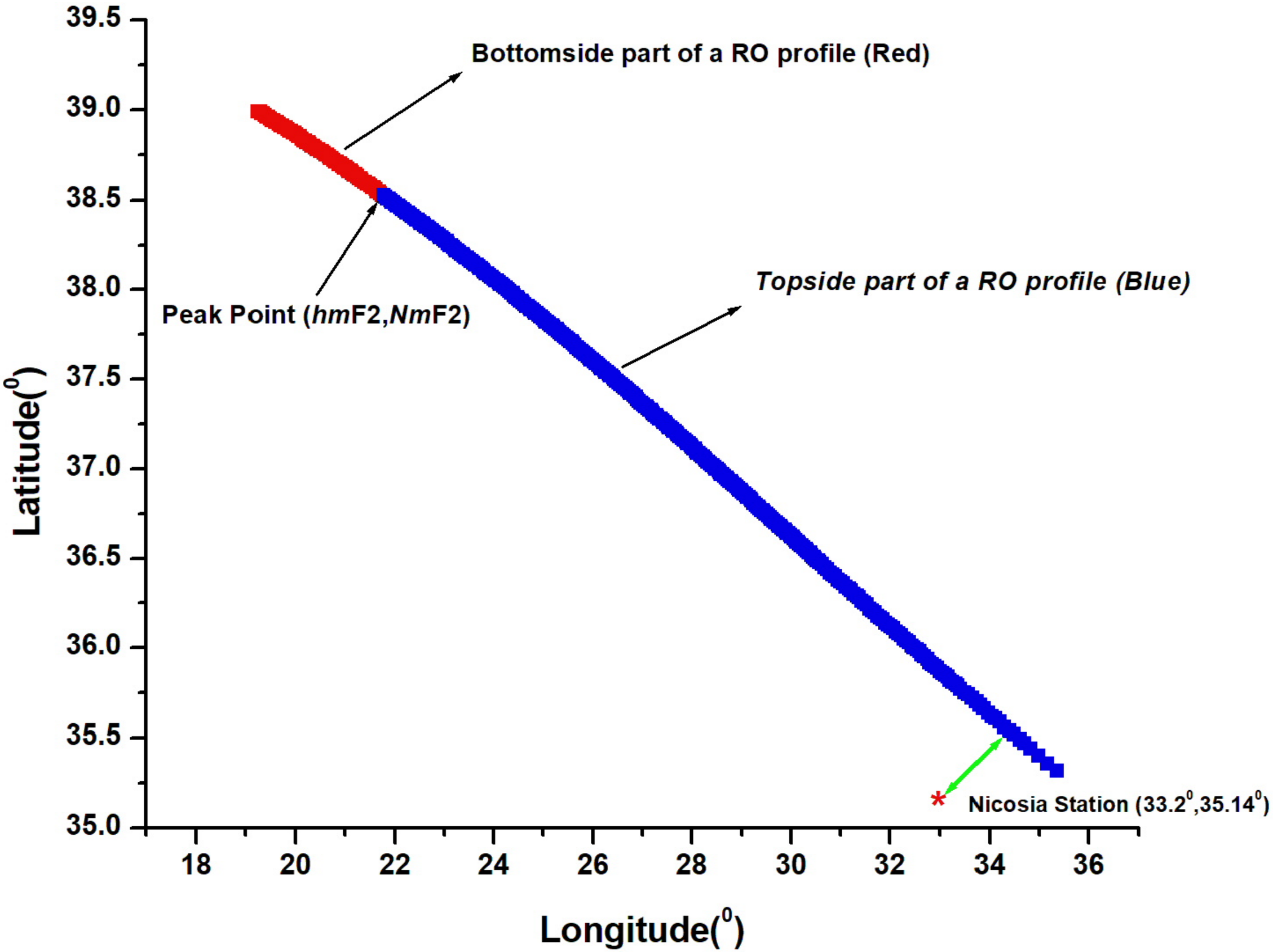
COSMIC RO profile projection coincident with nearest digisonde station at topside
Bottomside part of a RO profile (Red)
Peak Point (hmF2,NmF2)
Topside part of a RO profile (Blue)
Nicosia Station (33.2°,35.14°)
Latitude(°)
Longitude(°)
39.5
39.0
38.5
38.0
37.5
37.0
36.5
36.0
35.5
35.0
18
20
22
24
26
28
30
32
34
36

Figure 2.

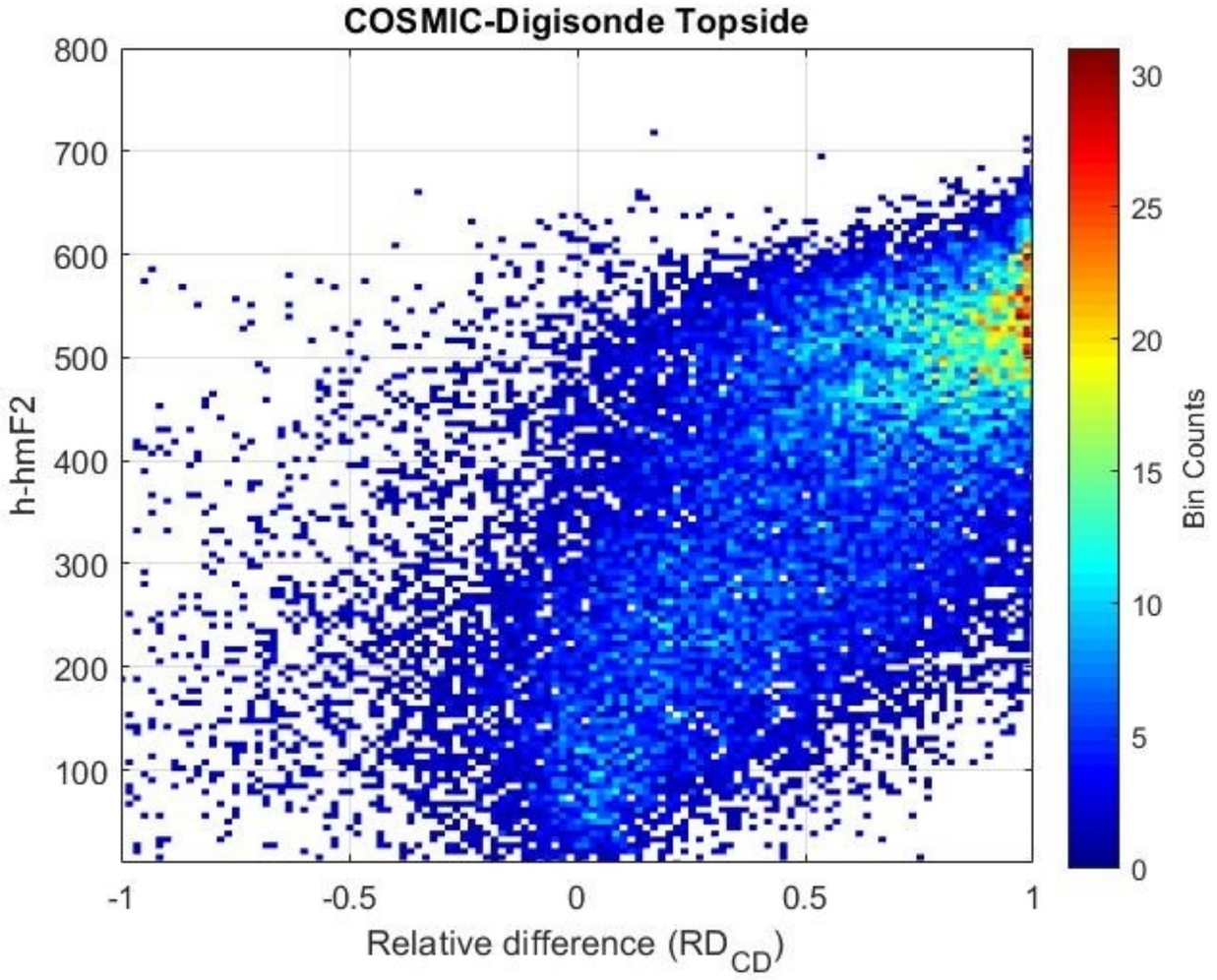
COSMIC-Digisonde Topside
h-hmF2
Relative difference (RD_CD)
Bin Counts
800
700
600
500
400
300
200
100
-1
-0.5
0
0.5
1
30
25
20
15
10
5
0

(a)

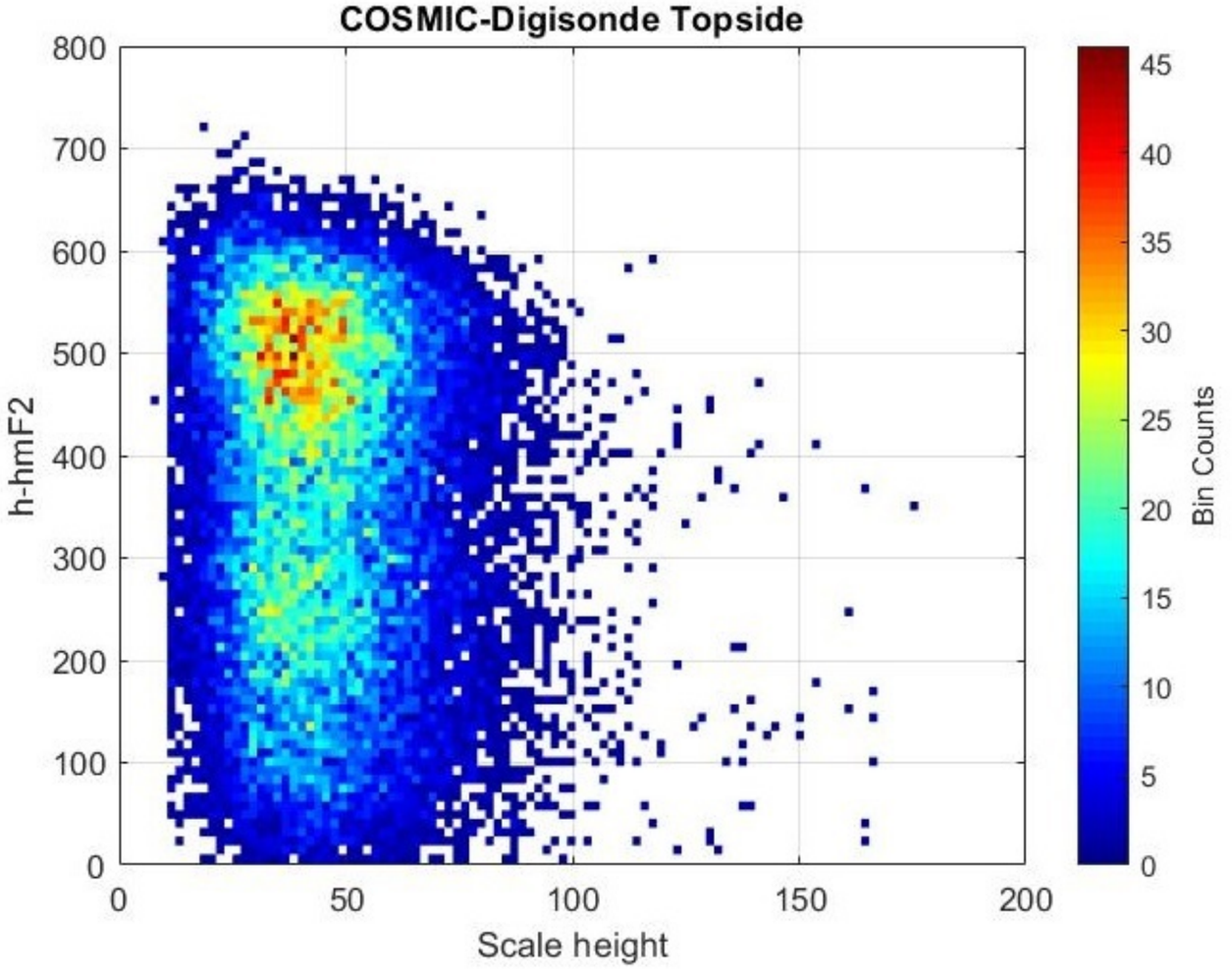
COSMIC-Digisonde Topside
h-hmF2
Scale height
Bin Counts
800
700
600
500
400
300
200
100
0
0
50
100
150
200
45
40
35
30
25
20
15
10
5
0

(b)

Figure 3.

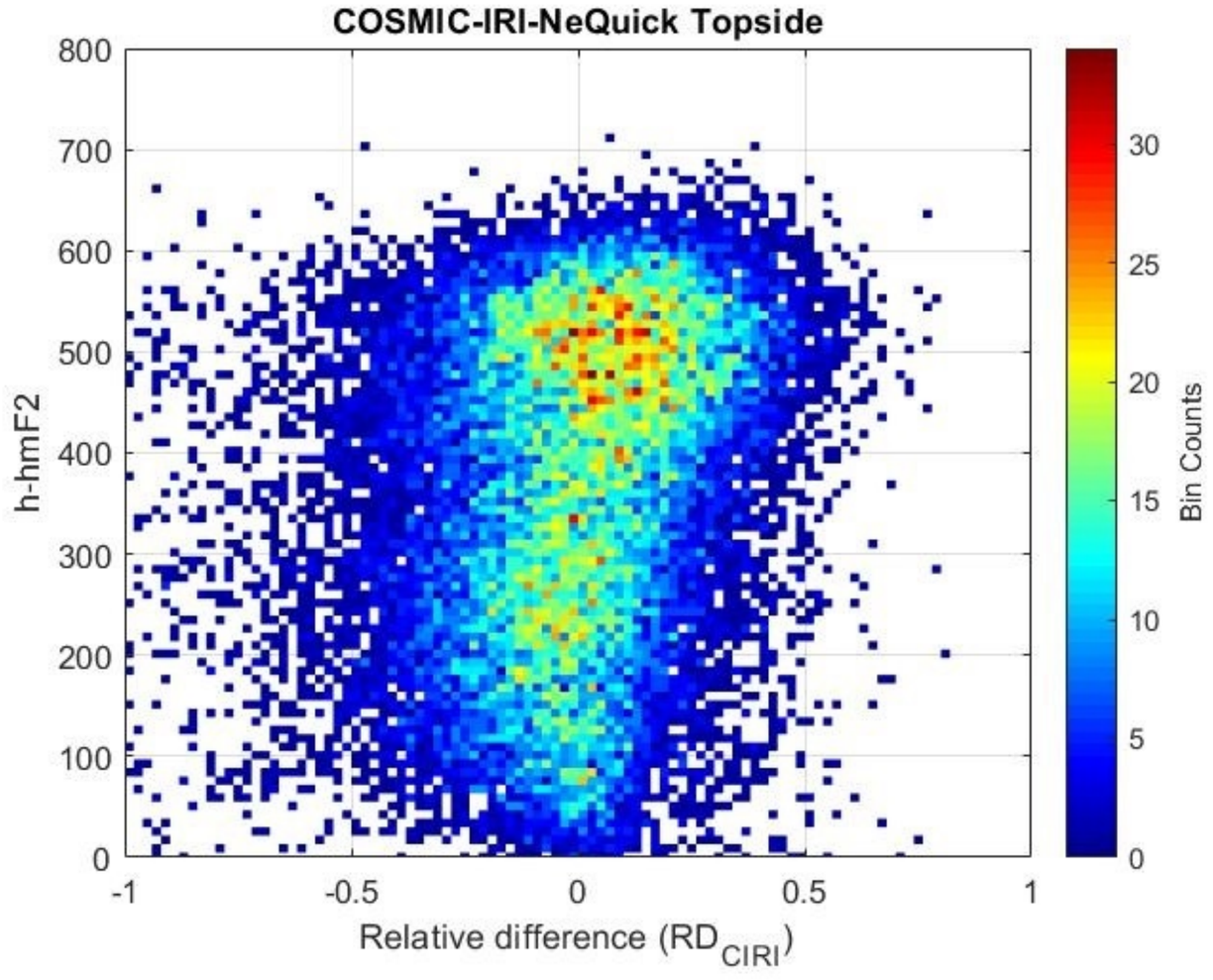
COSMIC-IRI-NeQuick Topside
h-hmF2
Relative difference (RD$_{CIRI}$)
Bin Counts
800
700
600
500
400
300
200
100
0
-1
-0.5
0
0.5
1
30
25
20
15
10
5
0

(a)

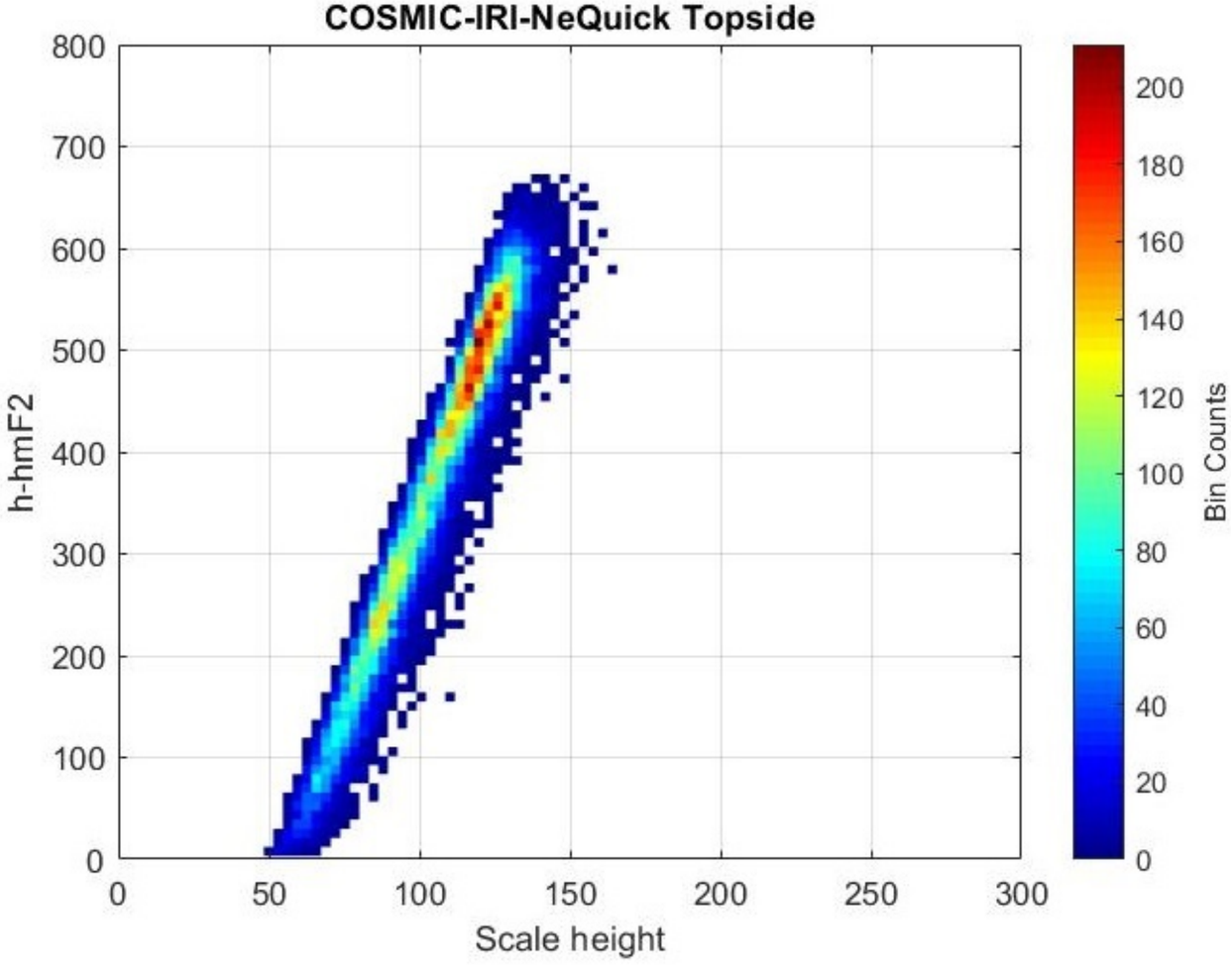
COSMIC-IRI-NeQuick Topside
h-hmF2
Scale height
Bin Counts
800
700
600
500
400
300
200
100
0
0
50
100
150
200
250
300
200
180
160
140
120
100
80
60
40
20
0

(b)

Figure 4.

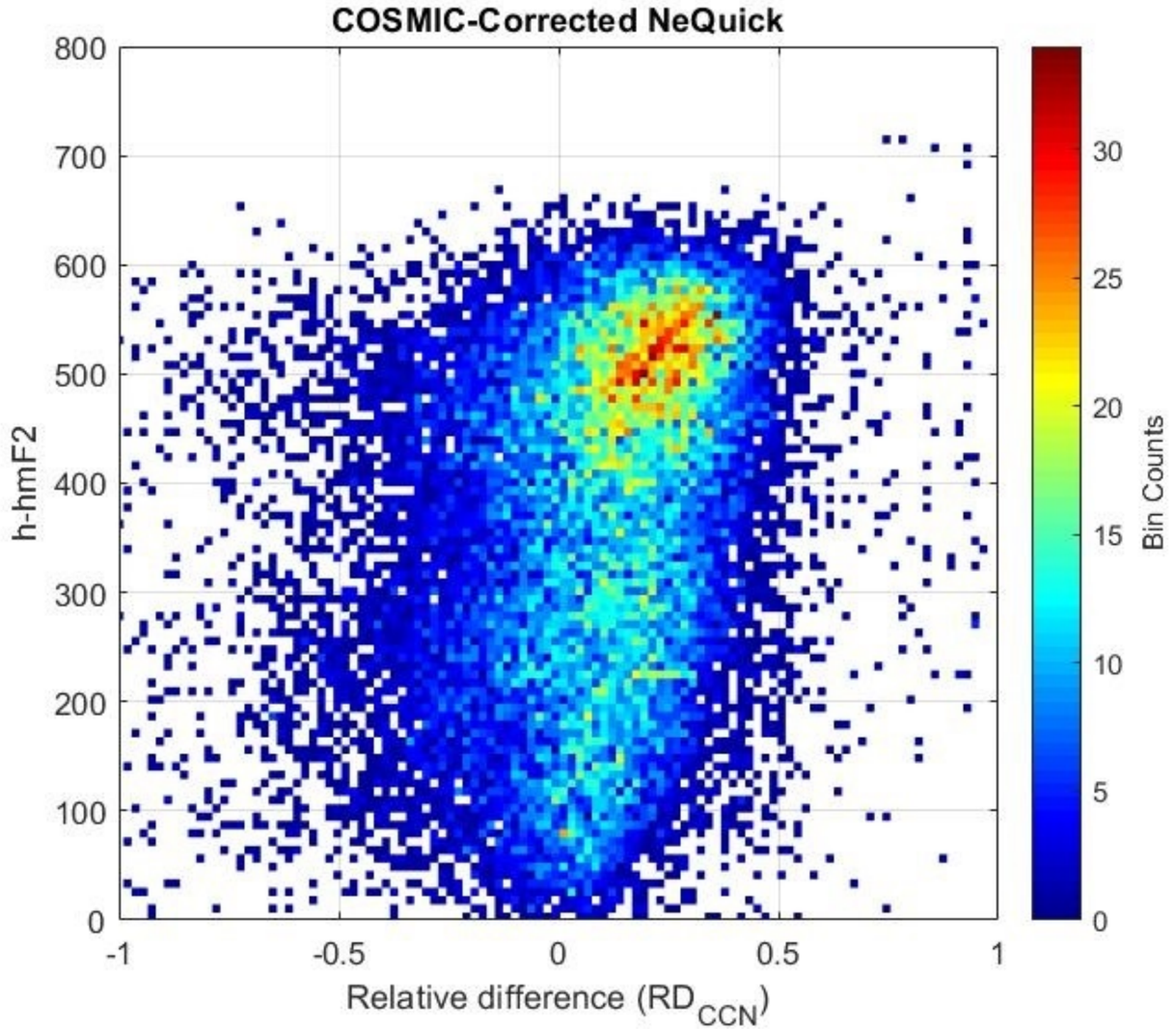
COSMIC-Corrected NeQuick
h-hmF2
Relative difference (RD$_{CCN}$)
Bin Counts
800
700
600
500
400
300
200
100
0
-1
-0.5
0
0.5
1
30
25
20
15
10
5
0

(a)

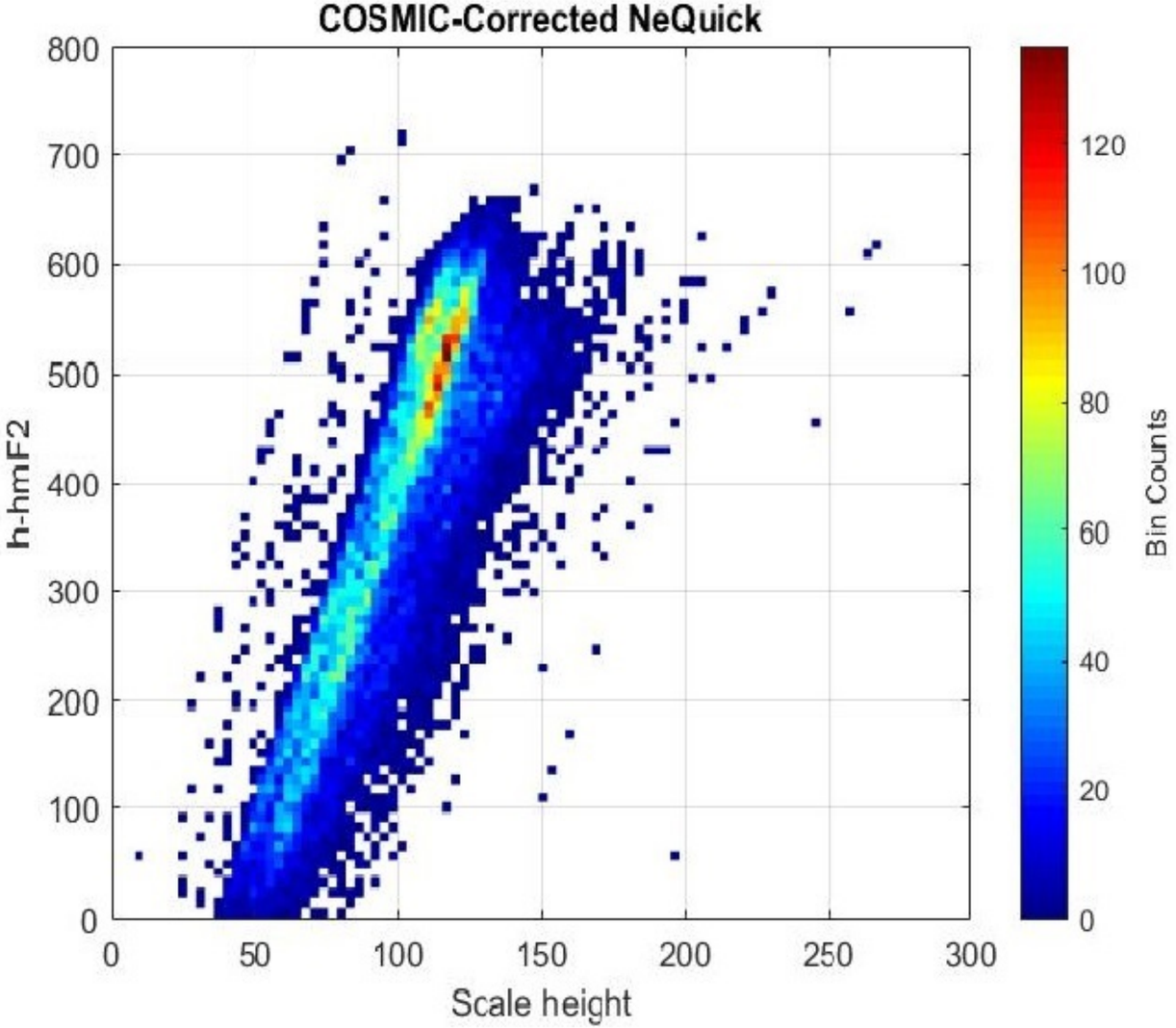
COSMIC-Corrected NeQuick
h-hmF2
Scale height
Bin Counts
800
700
600
500
400
300
200
100
0
0
50
100
150
200
250
300
120
100
80
60
40
20
0

(b)

Figure 5.

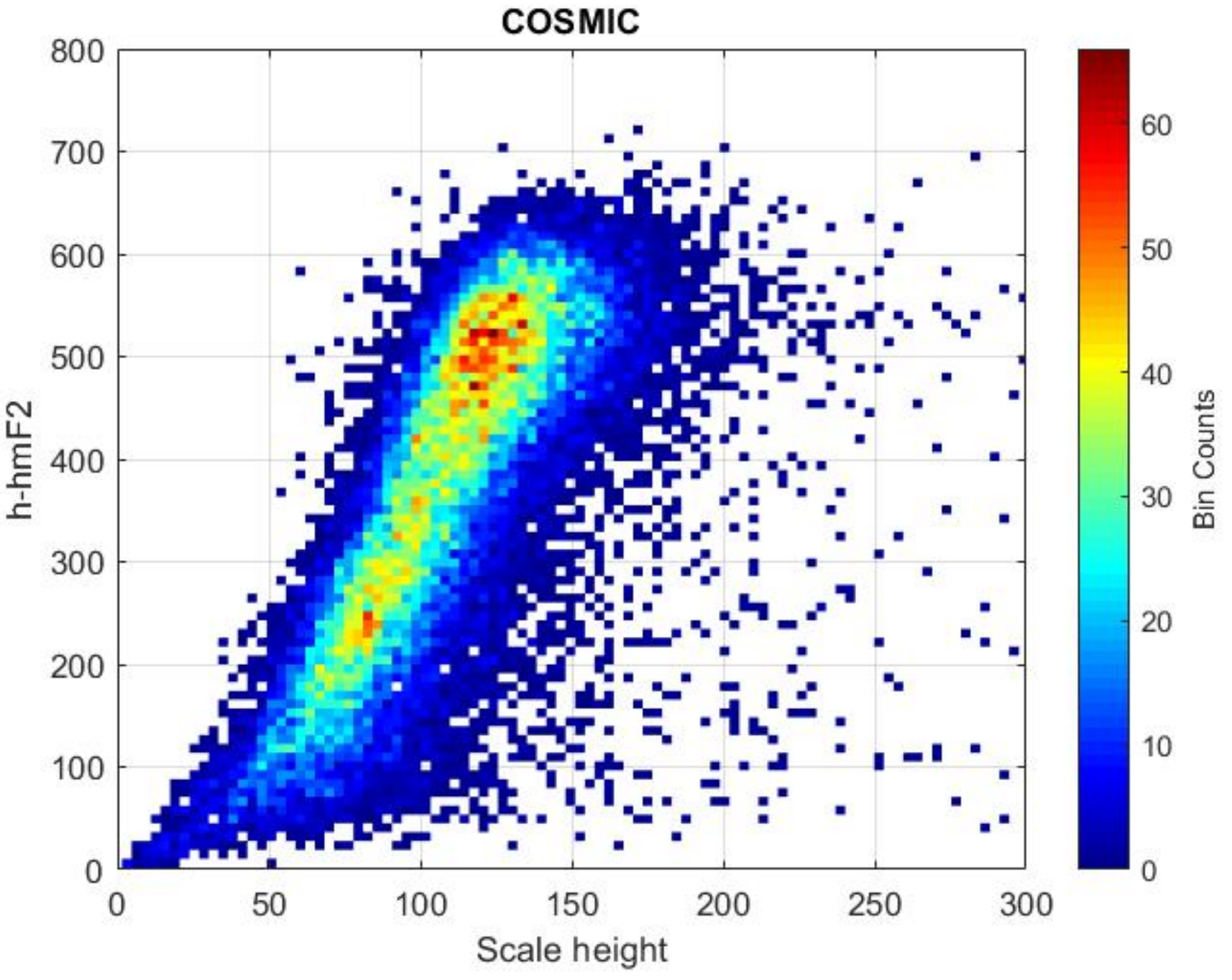
COSMIC
h-hmF2
Scale height
Bin Counts
800
700
600
500
400
300
200
100
0
0
50
100
150
200
250
300
60
50
40
30
20
10
0

Figure 6.

COSMIC-Corrected NeQuick

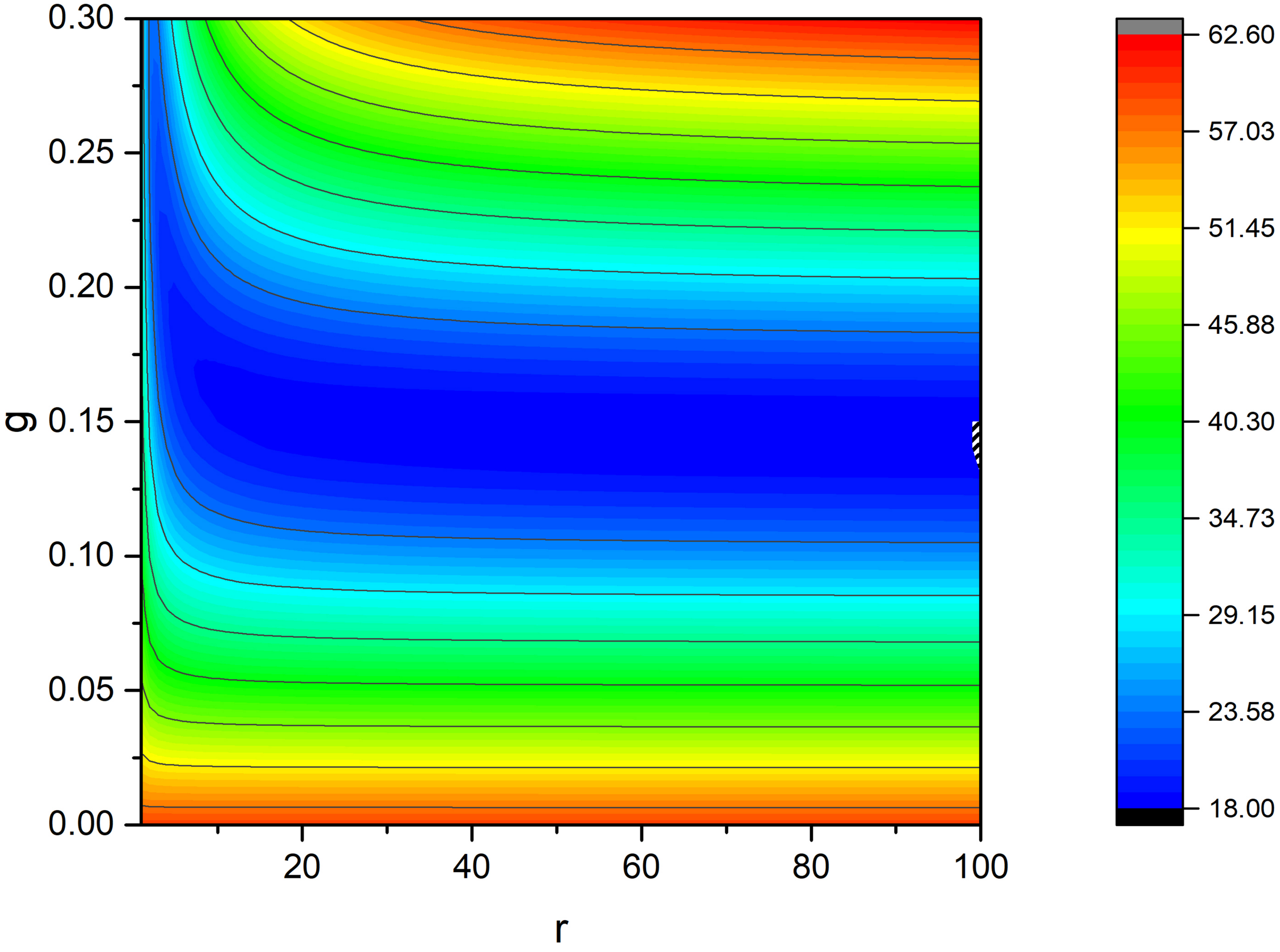

Figure 7.

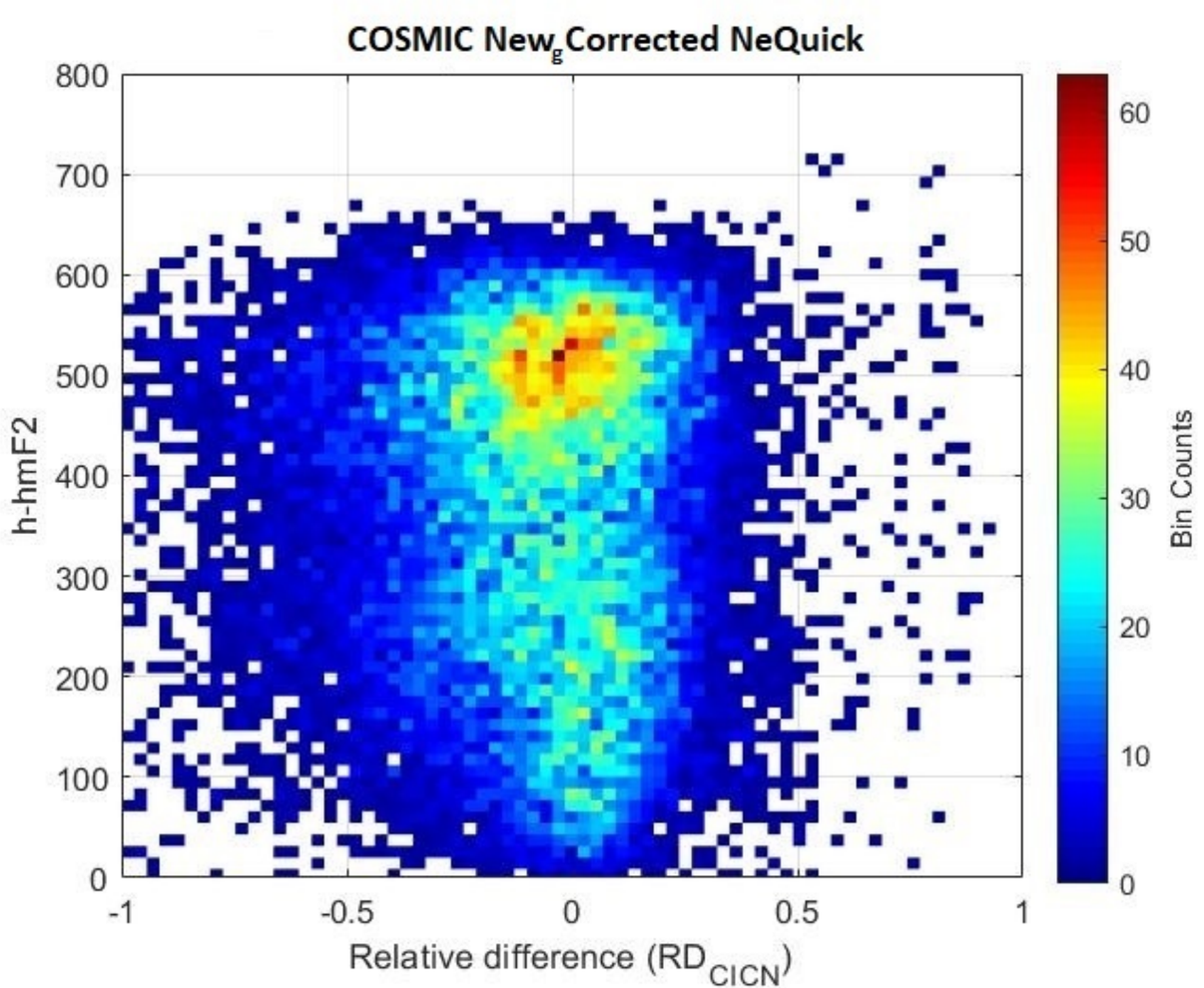
COSMIC New$_g$ Corrected NeQuick
h-hmF2
Relative difference (RD$_{CICN}$)
Bin Counts
800
700
600
500
400
300
200
100
0
-1
-0.5
0
0.5
1
60
50
40
30
20
10
0

(a)

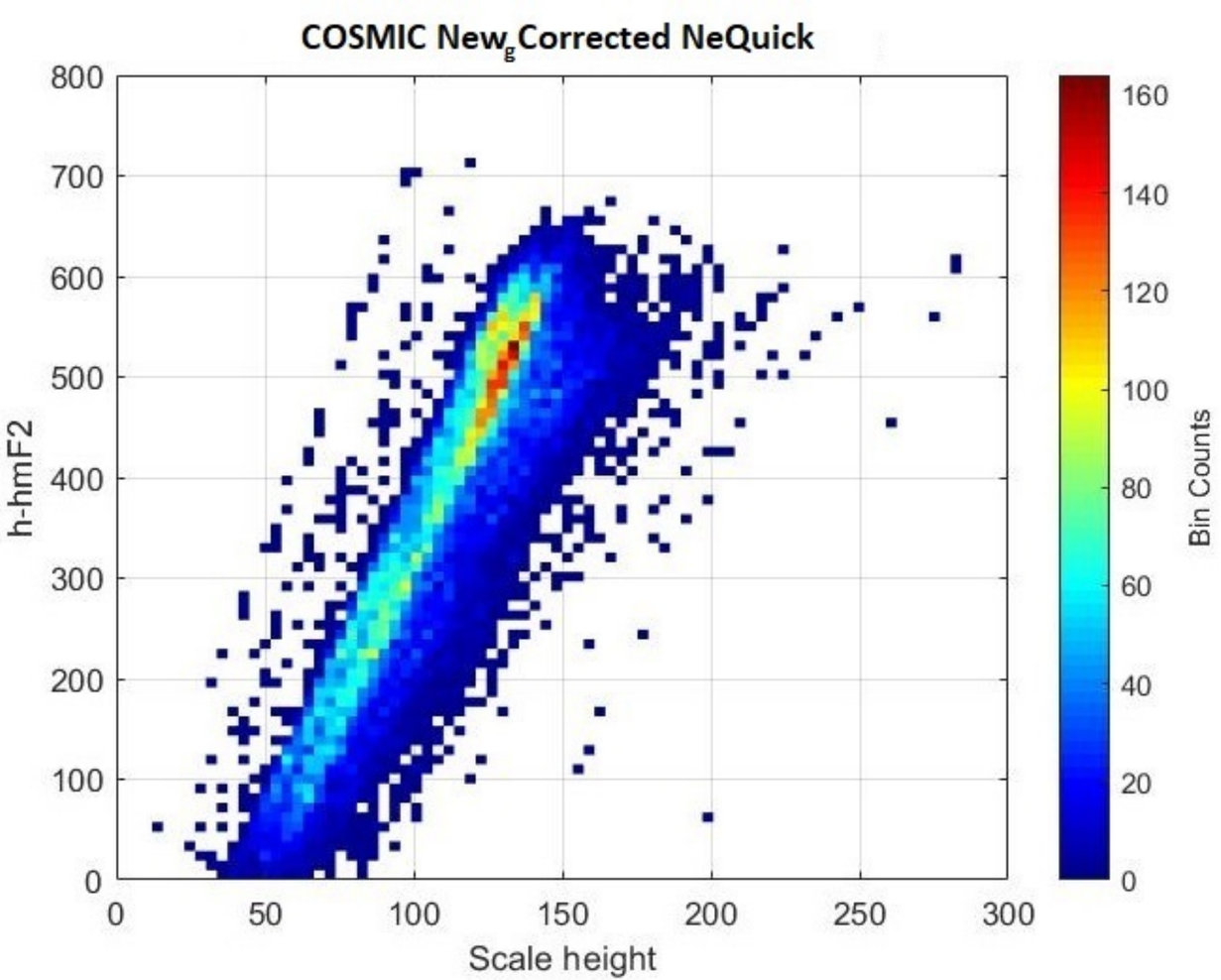
COSMIC New$_g$ Corrected NeQuick
h-hmF2
Scale height
Bin Counts
800
700
600
500
400
300
200
100
0
0
50
100
150
200
250
300
160
140
120
100
80
60
40
20
0

(b)

Figure 8.

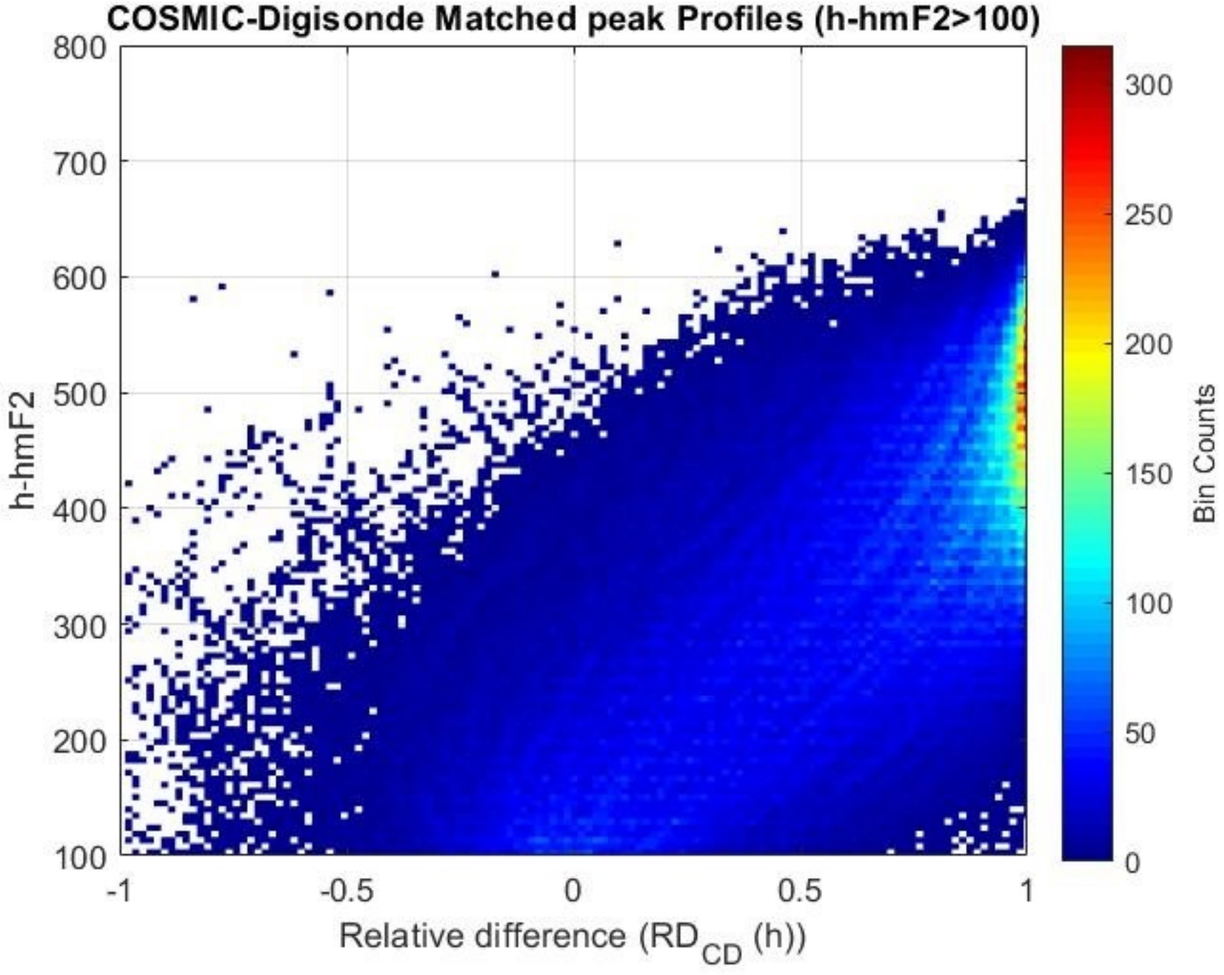
COSMIC-Digisonde Matched peak Profiles (h-hmF2>100)
h-hmF2
Relative difference (RD$_{CD}$ (h))
Bin Counts
800
700
600
500
400
300
200
100
-1
-0.5
0
0.5
1
300
250
200
150
100
50
0

(a)

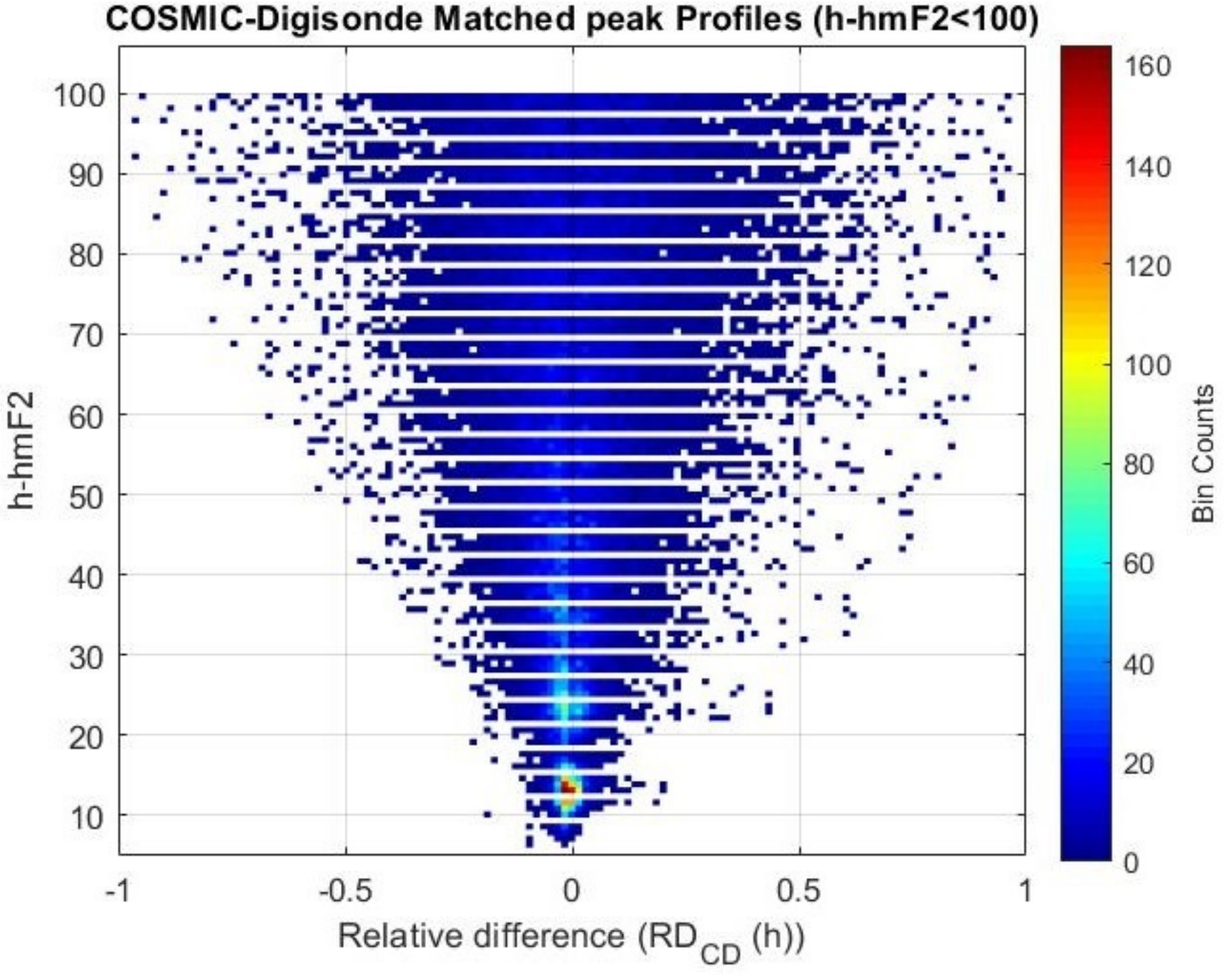
COSMIC-Digisonde Matched peak Profiles (h-hmF2<100)
h-hmF2
Relative difference (RD$_{CD}$ (h))
Bin Counts
100
90
80
70
60
50
40
30
20
10
-1
-0.5
0
0.5
1
160
140
120
100
80
60
40
20
0

(b)

Figure 9.

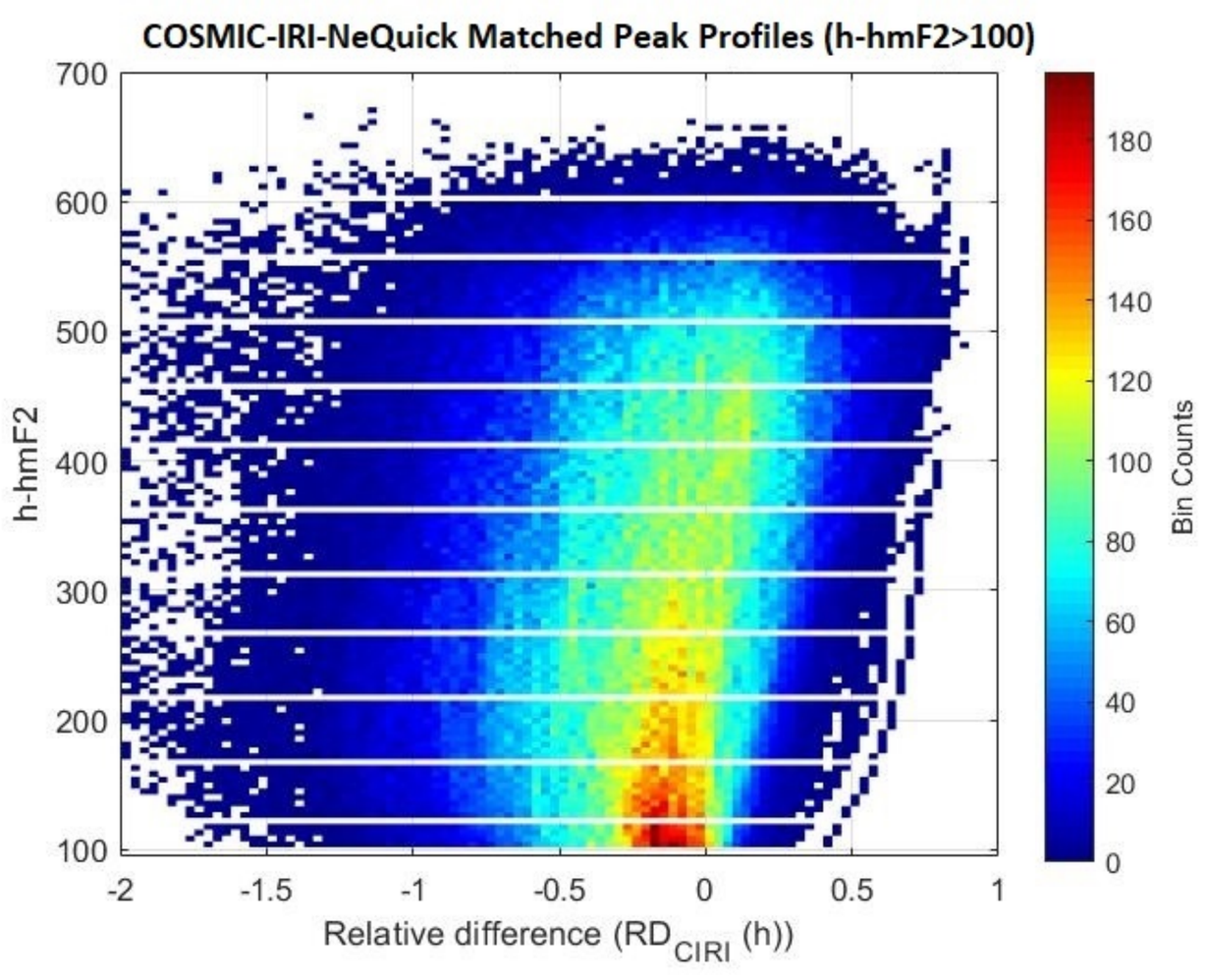
COSMIC-IRI-NeQuick Matched Peak Profiles (h-hmF2>100)
h-hmF2
Relative difference (RD CIRI (h))
Bin Counts
700
600
500
400
300
200
100
-2
-1.5
-1
-0.5
0
0.5
1
180
160
140
120
100
80
60
40
20
0

(a)

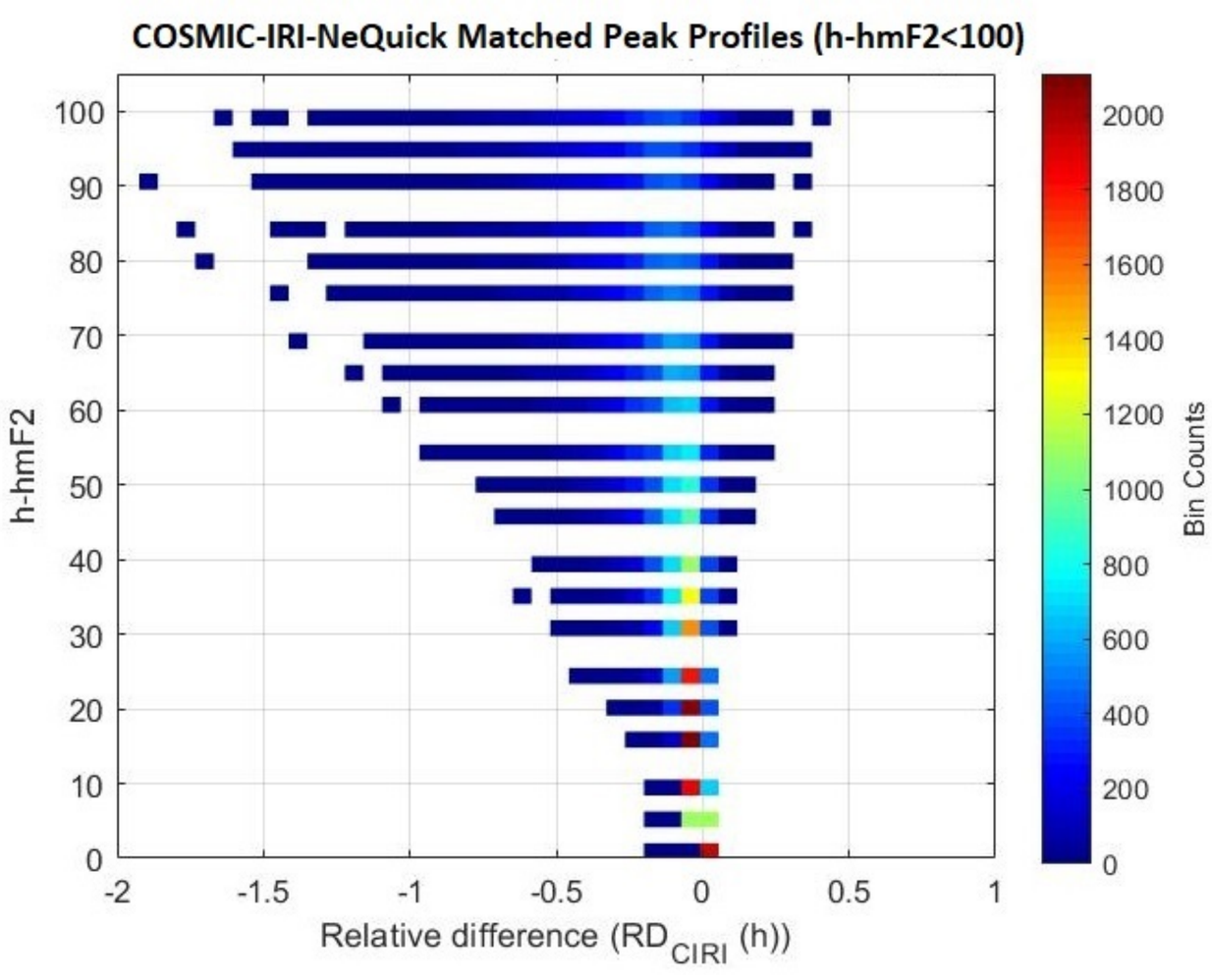
COSMIC-IRI-NeQuick Matched Peak Profiles (h-hmF2<100)
h-hmF2
Relative difference (RD CIRI (h))
Bin Counts
100
90
80
70
60
50
40
30
20
10
0
-2
-1.5
-1
-0.5
0
0.5
1
2000
1800
1600
1400
1200
1000
800
600
400
200
0

(b)

Figure 10.

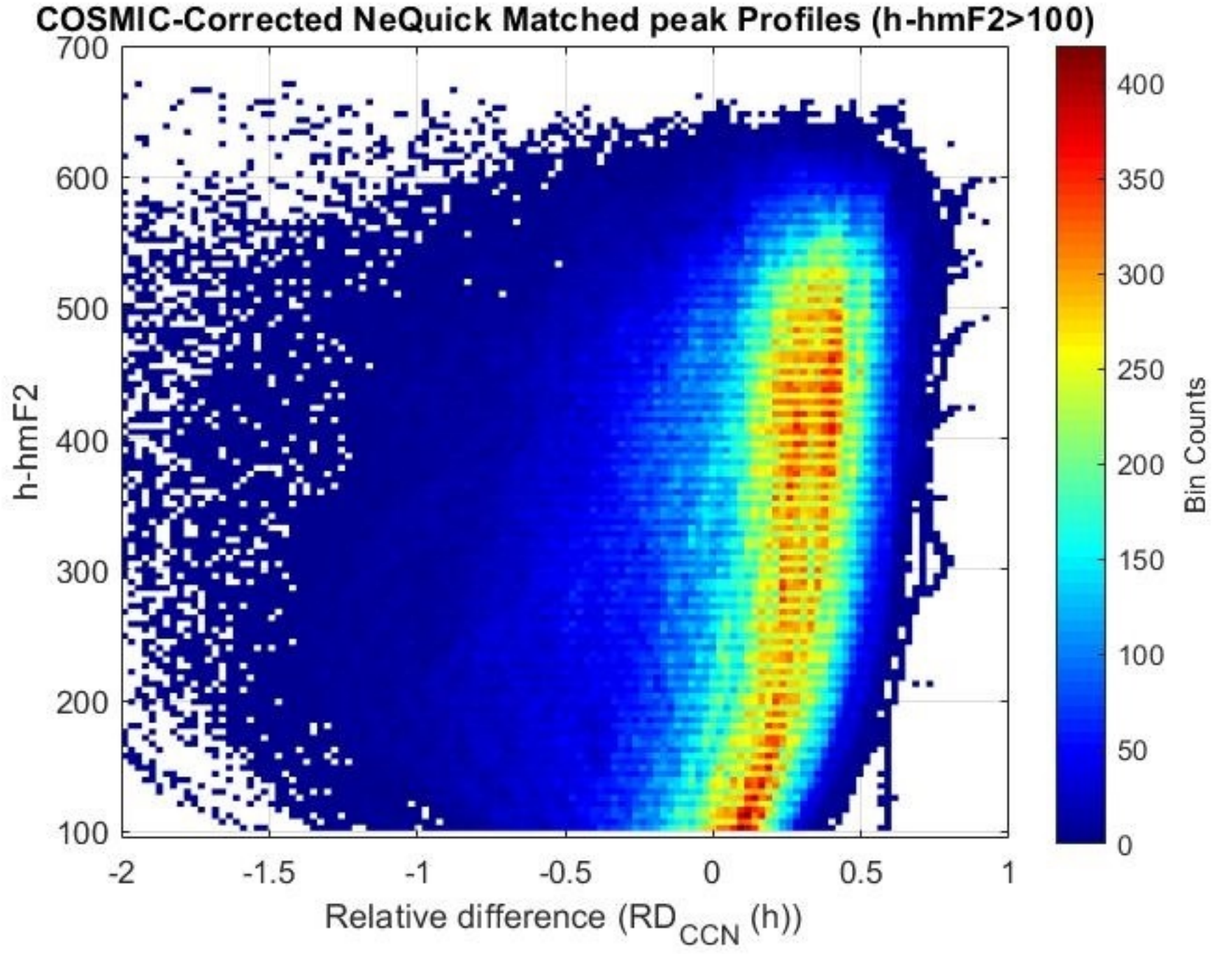
COSMIC-Corrected NeQuick Matched peak Profiles (h-hmF2>100)
h-hmF2
Relative difference (RD$_{CCN}$ (h))
Bin Counts
700
600
500
400
300
200
100
-2
-1.5
-1
-0.5
0
0.5
1
400
350
300
250
200
150
100
50
0

(a)

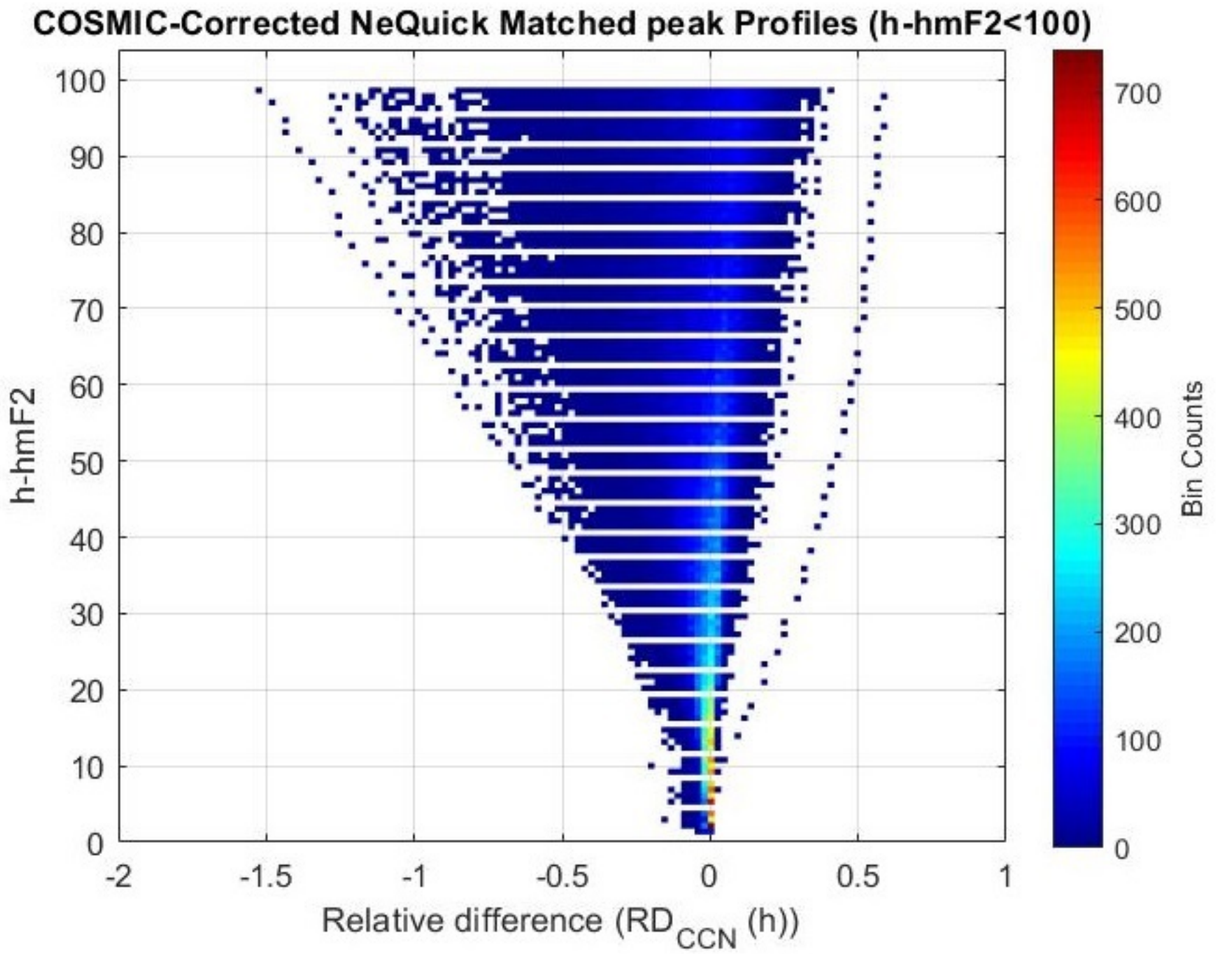
COSMIC-Corrected NeQuick Matched peak Profiles (h-hmF2<100)
h-hmF2
Relative difference (RD$_{CCN}$ (h))
Bin Counts
100
90
80
70
60
50
40
30
20
10
0
-2
-1.5
-1
-0.5
0
0.5
1
700
600
500
400
300
200
100
0

(b)

Figure 11.

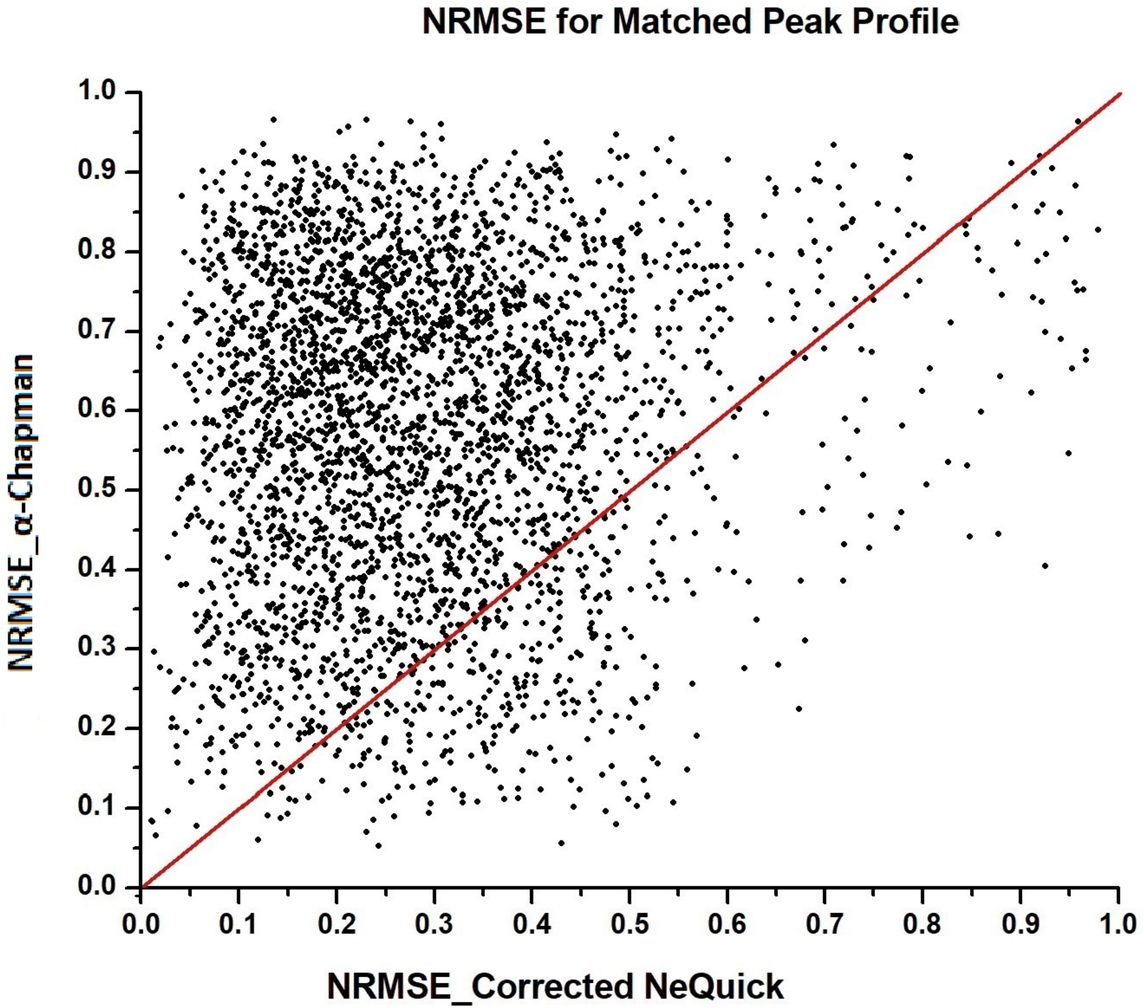
NRMSE for Matched Peak Profile
NRMSE_α-Chapman
NRMSE_Corrected NeQuick
0.0
0.1
0.2
0.3
0.4
0.5
0.6
0.7
0.8
0.9
1.0

(a)

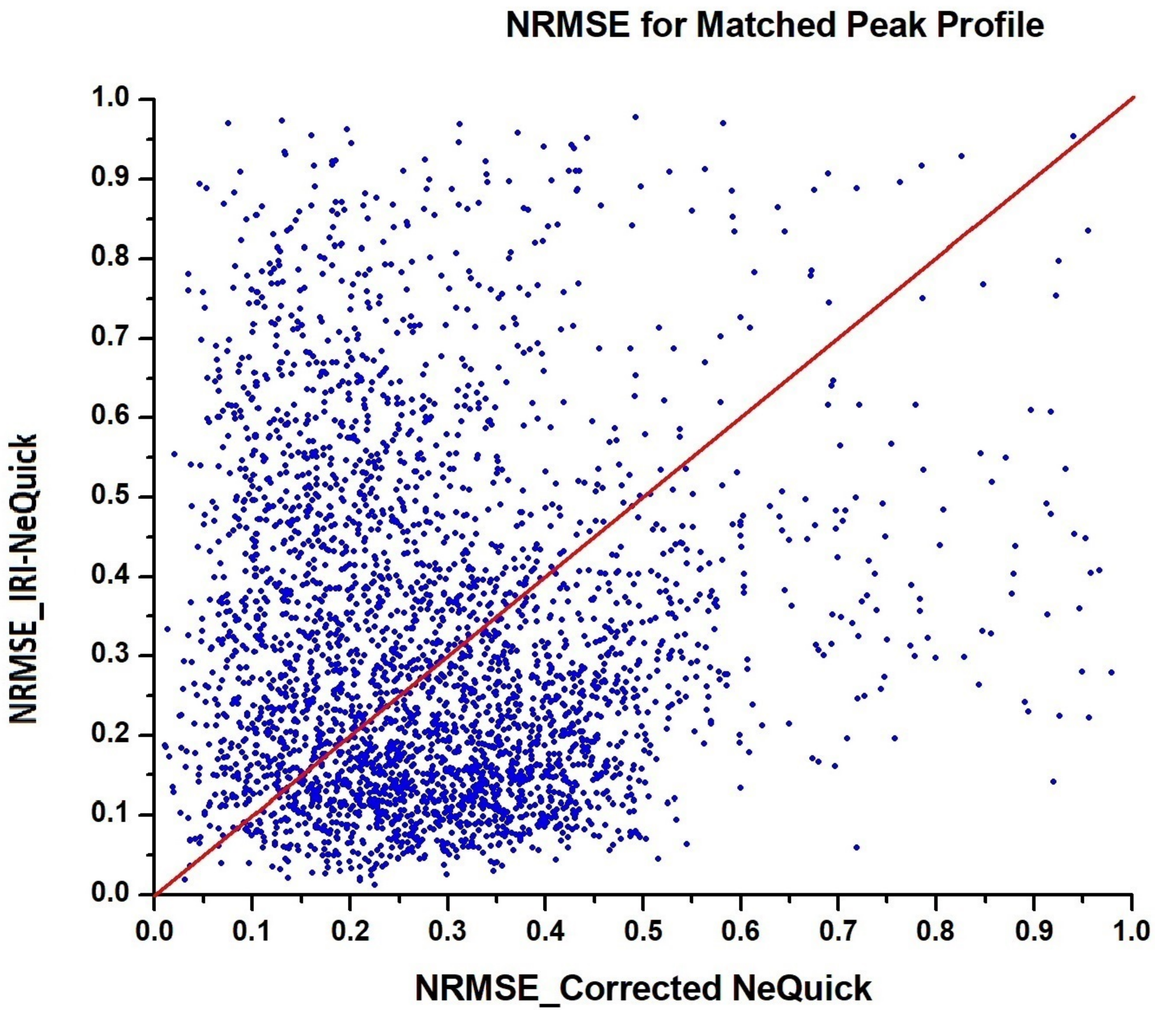
NRMSE for Matched Peak Profile
NRMSE_IRI-NeQuick
NRMSE_Corrected NeQuick
0.0
0.1
0.2
0.3
0.4
0.5
0.6
0.7
0.8
0.9
1.0

(b)

Figure 12.

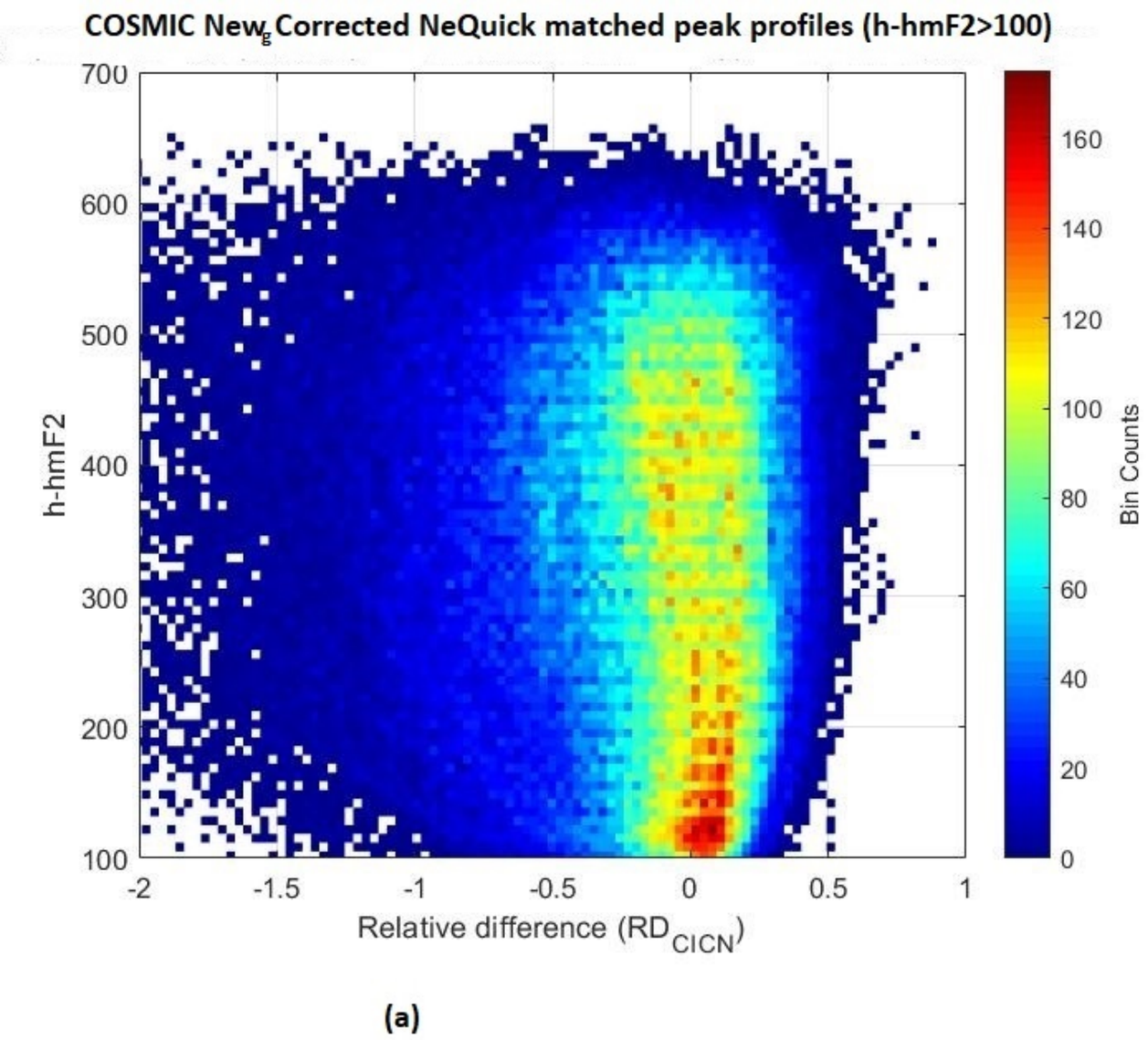
COSMIC New$_g$ Corrected NeQuick matched peak profiles (h-hmF2>100)
h-hmF2
Relative difference (RD$_{CICN}$)
Bin Counts
700
600
500
400
300
200
100
-2
-1.5
-1
-0.5
0
0.5
1
160
140
120
100
80
60
40
20
0

(a)

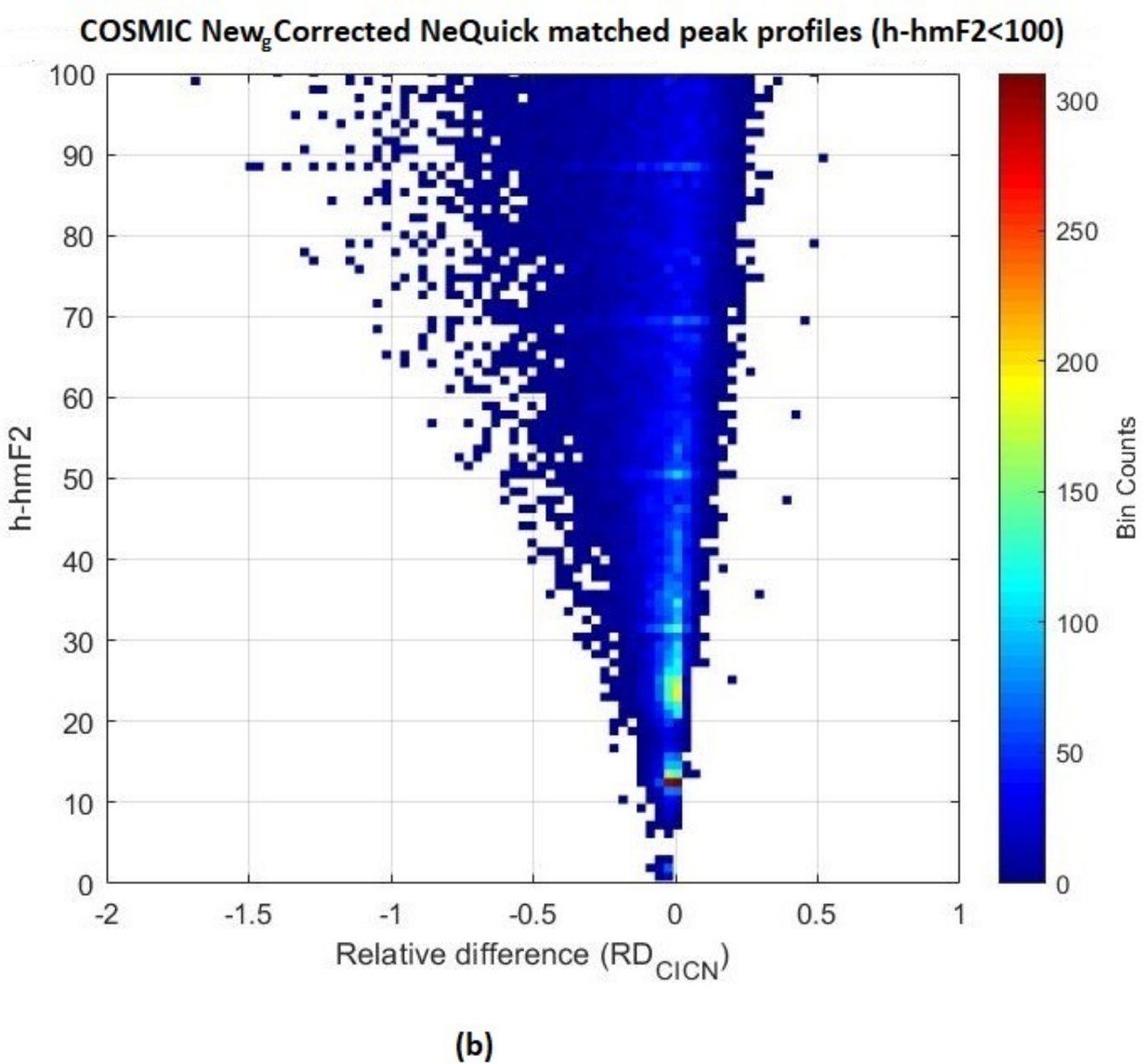
COSMIC New$_g$ Corrected NeQuick matched peak profiles (h-hmF2<100)
h-hmF2
Relative difference (RD$_{CICN}$)
Bin Counts
100
90
80
70
60
50
40
30
20
10
0
-2
-1.5
-1
-0.5
0
0.5
1
300
250
200
150
100
50
0

(b)

Figure 13.

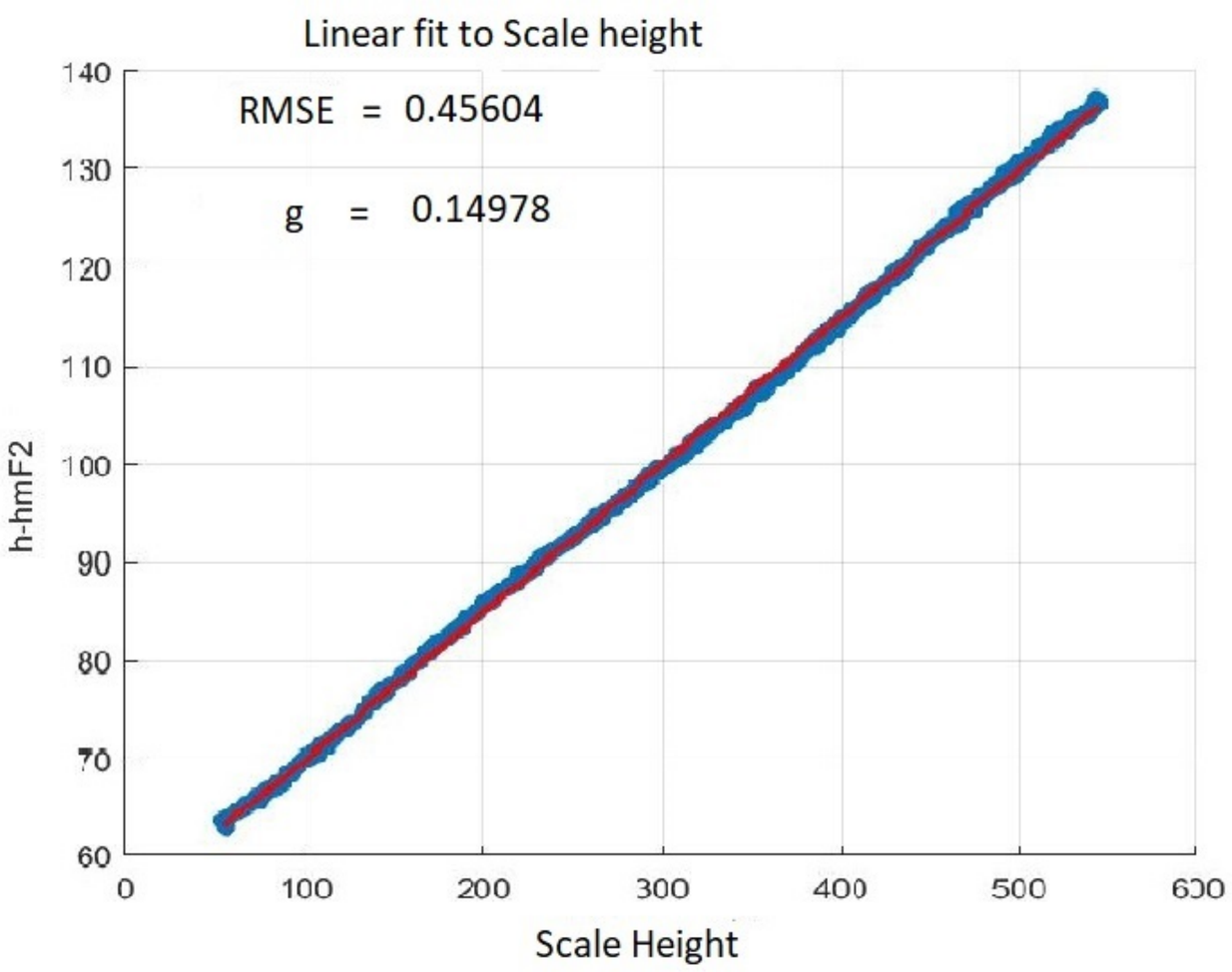
Linear fit to Scale height
RMSE = 0.45604
g = 0.14978
h-hmF2
Scale Height
140
130
120
110
100
90
80
70
60
0
100
200
300
400
500
600

(a)

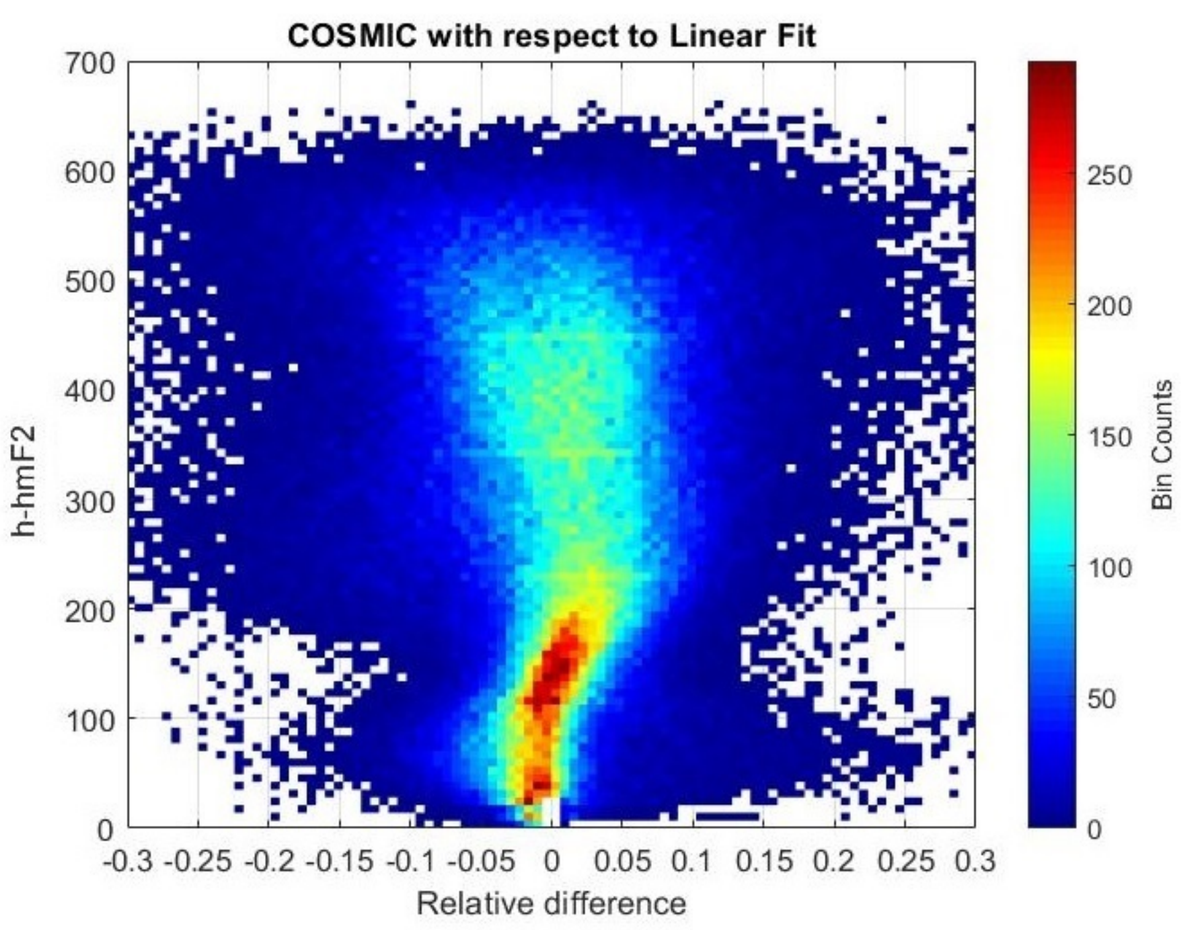
COSMIC with respect to Linear Fit
h-hmF2
Relative difference
Bin Counts
700
600
500
400
300
200
100
0
-0.3 -0.25 -0.2 -0.15 -0.1 -0.05 0 0.05 0.1 0.15 0.2 0.25 0.3
250
200
150
100
50
0

(b)

Figure 14.

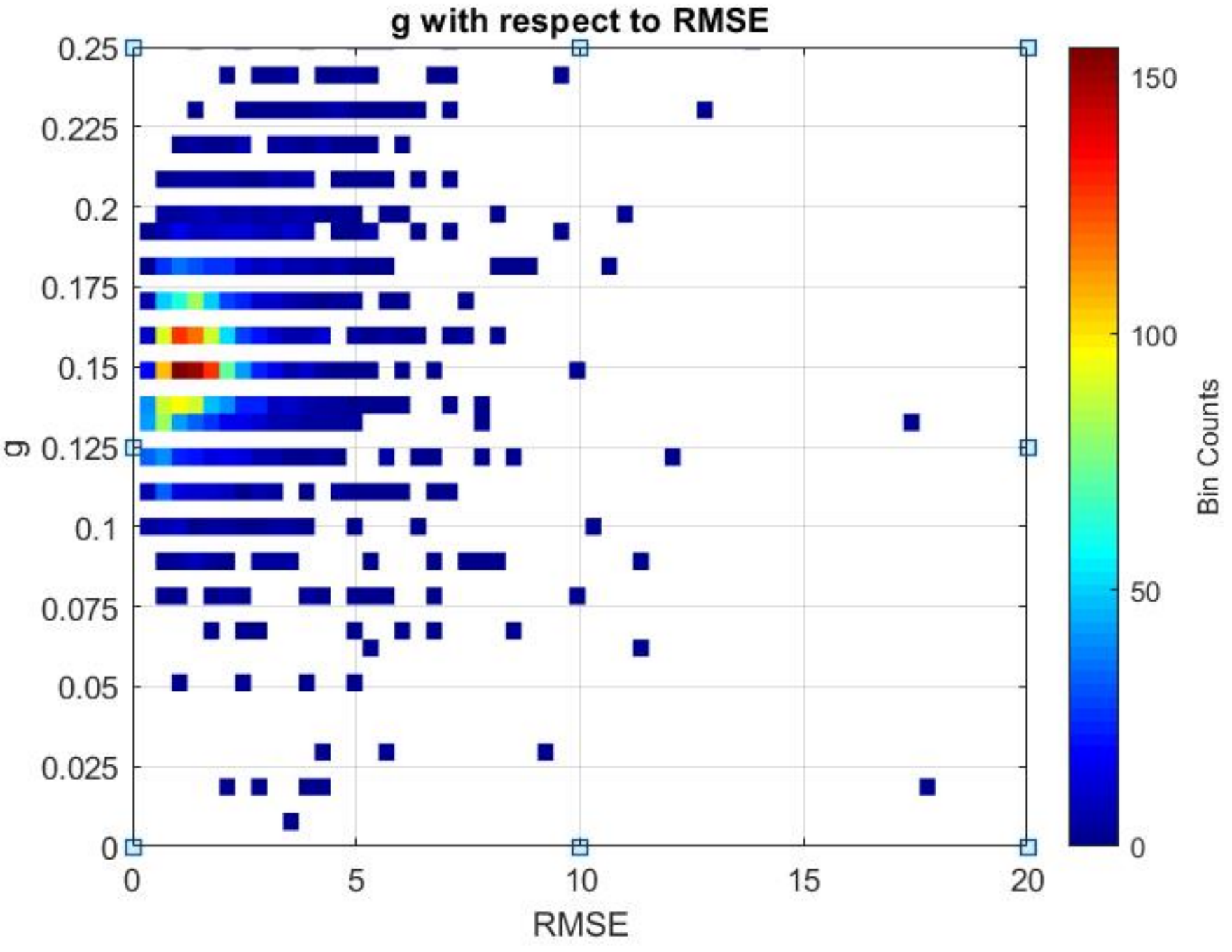
g with respect to RMSE
0.25
0.225
0.2
0.175
0.15
0.125
0.1
0.075
0.05
0.025
0
g
0
5
10
15
20
RMSE
150
100
50
0
Bin Counts

Table 1

Station name (Country)	Geog. Lat. (º)	Geog. Lon. (º)	Geo Mag. Lat.(º)	Number of Coincident observations	Number of Matched Peak Profiles
Alpena (Michaigan)	45.07	-83.56	46.94	93	8
Arenosillo (Spain)	37.1	-6.7	30.82	701	55
Arguello (USA)	34.8	-120.5	40.31	429	28
Ascension Island (UK)	-7.95	-14.4	-18.28	542	49
Athens (Greece)	38	23.5	31.98	997	75
Austin (USA)	30.4	-97.7	32.60	238	55
Boa (Brazil)	2.88	60.7	5.62	46	2
Boulder (USA)	40	-105.3	48.35	1057	126
Dourbes (Belgium)	50.1	4.6	45.90	1637	249
Eielson (Alaska)	64.6	-147.7	65.65	224	33
Fortaleza (Brazil)	-3.9	-38.4	-6.41	234	14
Gakona (USA)	62.4	-145	62.99	1246	101
Goose Bay (Canada)	62.38	-145	60.46	229	30
Grahamstown (South Africa)	-33.3	26.5	-41.38	950	96
Guam	13.6	144.86	16.13	85	14

Hermanus (South Africa)	-34.42	19.22	30.99	885	164
ICheon (South Korea)	37.14	127.54	39.20	478	60
Idaho (USA)	43.81	-112.67	45.71	379	59
Jeju (South Korea)	33.43	126.3	26.81	562	83
Jicamarca (Peru)	-12	-76.8	0.09	283	12
Juliusruh (Germany)	54.6	13.4	50.71	1141	163
Kwajalein (Marshall isl.)	9	167.2	3.85	235	16
Learmonth (Australia)	-21.8	114.1	-32.25	607	65
Louisvale (South Africa)	-28.5	21.2	-37.67	688	100
Madimbo (South Africa)	-22.39	30.88	-32.33	1668	224
Millstone Hill (USA)	43.6	-71.5	51.77	1637	186
Moscow (Russia)	55.5	37.3	51.34	614	102
Nicosia (Cyprus)	35.14	33.2	29.23	468	27
Nord (Greenland)	81.4	-17.5		43	1
Pruhonice (Czech Republic)	50	14.6	45.49	1230	288
Ramey (Puerto Rico)	18.5	-67.1	27.59	390	57
Rome	41.9	12.5	36.03	858	108

(Italy)					
Roquetes (Spain)	40.8	0.5	34.98	1307	160
King Salmon (USA)	58.4	-156.4	56.89	795	87
Sanya (China)	18.34	109.42	20.78	124	3
Sao Luis (Brazil)	-2.6	-44.2	-2.27	203	12
Sondrestrom (Greenland)	66.98	-50.94	72.28	610	46
Port Stanley (Falkland isl.)	-51.6	-57.9	-38.88	1376	155
Thule (Greenland)	76.54	-68.44	76.05	143	11
Tromso (Norway)	69.58	19.22	66.52	897	135
San Vito (Italy)	40.6	17.8	34.73	758	104
Wallops Island (USA)	37.94	-75.58	47.83	1318	09
Wuhan (China)	30.5	114.4	32.70	75	10
Yakutsk (Russia)	62	129.6	56.33	583	51
Total				**29,063**	**3433**